ARTICLES

$\pi\pi$-angular correlations for $\pi^- p \rightarrow \pi^+\pi^- n$ in the region of the Δ dominance

R. Müller, R. Baran, U. Bohnert, P. Helbig, G. Herrmann,
A. Hofmann,* O. Jäkel, H. Krüger, D. Malz, W. Menzel,
H.-W. Ortner, L. Schweinzer, and S. Wirth
Physikalisches Institut der Universität Erlangen, Erwin-Rommel-Strasse 1, D-8520 Erlangen, Germany
(Received 11 June 1992; revised manuscript received 3 May 1993)

The reaction $\pi^- p \rightarrow \pi^+\pi^- n$ was studied at a total c.m. energy of 1301 MeV. The incoming pion beam was focused on a liquid hydrogen target. For the π^+ detection a large acceptance spectrometer was used whereas the outgoing π^- was measured in a 4 sr detector arrangement. A collected set of 32 000 kinematical complete $\pi^- p \rightarrow \pi^+\pi^- n$ events delivered invariant mass distribution and double differential cross sections as well as angular correlation functions and triple differential cross sections, respectively. The observables, showing a characteristic deviation from phase space, are compared with model calculations based on Weinberg's Lagrangian. The dynamics of the reaction is well described. In addition, there are clear indications for the need of relativistic corrections, whereas the data do not justify strong contributions of σ- and ρ-propagation diagrams.

PACS number(s): 13.75.Gx, 11.40.Fy, 13.75.Lb

I. INTRODUCTION

A. Theoretical motivation

Nowadays, QCD, the well-established gauge field theory of strong interacting particles, is widely believed to be the correct fundamental theory of hadron physics. A test of the theoretical implications of the QCD Lagrangian is, however, restricted to high energy processes, where the perturbative methods work. The low energy behavior of QCD, which more directly exhibits the most interesting feature, namely confinement, is far from being well understood. Therefore, several attempts have been made to formulate phenomenological models using mesonic and nucleonic degrees of freedom rather than quarks and gluons, but respecting the fundamental symmetries of QCD. Such attempts are, for example, the bag models [1], Lagrangians based on current algebra [2], and chiral perturbation theory [3]. What has been learned from these models so far is at least one fact: Chiral symmetry plays a crucial role in low energy hadron physics, as it induces nonlinear $\pi\pi$ and πN interactions. Therefore, the natural testing ground for low energy QCD-"inspired" models is and has been $\pi\pi$ scattering. Excellent information on the $\pi\pi$ interaction is obviously gained by the study of pionic pion production, where the final state interaction is dominated by the $\pi\pi$-scattering amplitude. In other words, the characteristics of the $\pi N \rightarrow \pi\pi N$ reactions is the $\pi\pi$ amplitude involved already in lowest order of the perturbation expansion.

The total cross section data in the region of threshold provide a first crude insight into the validity of the models. However, refined analysis based on the Weinberg Lagrangian [4], taking into account $\pi\pi$-final-state interaction, πN rescattering, relativistic effects, etc. only makes sense if it can be tested by detailed experimental information. Therefore, a test of various models must be performed on more exclusive data. An advanced study is provided by the triple differential cross section (or alternatively by angular correlation functions) in the region of the Δ resonance, where interferences of nonlinear diagrams with Δ-dominated amplitudes provide a sensitive test to the models. At higher energies around and above the Roper resonance, the baryonic degrees of freedom start to dominate over the nonlinear pion-pion coupling. This limits the useful energy region for pion production experiments to $E_{\text{c.m.}} \leq 1400$ MeV.

B. Experimental review

During the last 30 years, several $(\pi, 2\pi)$ data have been published at energies below the Roper resonance [5–14]. Most of these data correspond to the $\pi^- p \rightarrow \pi^+\pi^- n$ reaction. In detail, the first data were a couple of individual events observed in emulsion experiments at various energies for the incoming pion. Unfortunately, only some hundred kinematically complete events of the considered channel of the $(\pi, 2\pi)$ reaction below $E_{\text{c.m.}} = 1400$ MeV were observed. The data of bubble chamber experiments also suffer from low statistics, but yielded a first insight

*Deceased.

into the angular and momentum distributions [5, 6, 8, 9].

Later on, other measurements [7, 10–12] delivered more inclusive data like the double differential cross section $d^2\sigma/d\Omega dT$ for the produced π^+ with better statistics. These data are based on single arm spectrometer experiments. In addition, total cross sections were measured with good statistics [11, 12]. Recently, a more precise experiment at CERN was published: the OMICRON experiment measured kinematically complete events by observing both outgoing pion tracks in the scattering plane. The OMICRON experiment mainly published total cross sections and invariant mass data with reasonable statistics [14].

However, presently no triple differential cross section or similar exclusive data for a detailed analysis of the reaction dynamics are available. An experiment to fill this gap was presented in Ref. [15]. Here we want to outline the details of this experiment and report about some of the results.

C. Aim of the experiment

The aim of this experiment was to provide triple differential cross sections with good statistics for the reaction $\pi^- p \rightarrow \pi^+\pi^- n$. Full exclusive data, reflecting the five independent kinematical degrees of freedom of a three-body reaction, require an enormous amount of events to fill each interval of the adequately segmented 5-dimensional phase space with a reasonable number of counts.

At least, the measurement should cover a reasonable part of the phase space to allow a comparison with a model at various kinematical conditions. To estimate the influence and energy dependence of the contributing diagrams (especially of the linear and nonlinear terms referring to [16, 17]), the measurements were done at different energies close to threshold, where the pole term (referring to [16, 17]) is expected to dominate. In- and out-of-plane data for the (π^+, π^-, n) system are very important to test the influence of particular diagrams.

For experimental reasons, which will be described in the following sections, a feasible lower limit in energy for this experiment was expected around $E_{\rm c.m.} = 1274$ MeV (i.e., 54 MeV above threshold).

D. Idea of the measurement

Up to the kinetic energy of $T_{\pi^-}^{\rm lab} \approx 350$ MeV the reaction $\pi^- p \rightarrow \pi^+\pi^- n$ is the only one which can produce a positive pion using a beam of negative pions and a hydrogen target. Since other target materials than hydrogen allow the π^+ production at these energies via other reaction mechanisms, like double charge exchange (DCX), the experimental target should consist of pure hydrogen.

Using a pure hydrogen target, the detection of a positive pion, which appeared coincidently with an incoming single π^- of the beam served as an unique tagging of the reaction.

A dipole magnet was used as a charge filter and spectrometer for the emitted positive particles. After having passed the magnetic field, the particles were stopped in a scintillator stack which allowed to search for the characteristic decay cascade of positive pions. The emission of the positive pion identifies the reaction. When the reaction was identified, the other coincident charged particle must have been a π^-.

Since the input parameters, like beam momentum and particle masses, are well known, at least five independent observables were necessary for a kinematically complete measurement of this reaction. Beside the obviously difficult identification of the π^+, the three-momentum of the particle was determined. The detection of the charged π^- delivered the two missing observables: the polar and the azimuthal angle.

II. DESCRIPTION OF THE SETUP

A. Experimental environment

The experiment was performed at the πM1 channel of the Paul-Scherrer Institute (PSI, Switzerland). The pions were produced by a 590 MeV proton beam hitting the target station M [18]. The particles of the secondary beam showed the time structure of the proton beam: bursts of less than 1 ns with a separation of 20 ns, what was convenient for coincidence experiments. The 20 m long secondary beamline allowed a discrimination between the different components by time of flight (TOF). A fraction of more than 90% pions on the target at a π^--beam momentum of 400 MeV/c was achieved. A hodoscope in the intermediate focus of the beamline gave information about the exact momentum ($\pm$ 200 keV/c at 400 MeV/c) for each beam particle. Additionally, it provided information on the number of beam-line pions for each cyclotron burst.

B. Target

The pion beam was focused on a liquid hydrogen (LH_2) target, a 90 mm long Mylar cylinder, 60 mm in diameter with the rotation axis along the beam direction. This led to a mass density of 630 mg/cm^2 hydrogen. The cell was built of 100 μm thick Mylar foils, which were pressed into a mould at 100 °C. The vacuum vessel was made of carbon fibers [19]. This special device was necessary for keeping the multiple scattering of the produced low energy pions as small as possible. A prototype vessel, which had a mass density of approximately 180 mg/cm^2 [19] and a final version with a mass density of 100 mg/cm^2 for the spherical wall was used during different periods of measurement. The advantage of this construction was the combination of low mass density and low atomic number of the wall materials. Both items reduced multiple scattering. The continuous low mass density was achieved for a solid angle of nearly 4π sr. A cross section of the vessel and target cell is shown in Fig. 1. Two windows of Kapton foil were mounted for the particle beam.

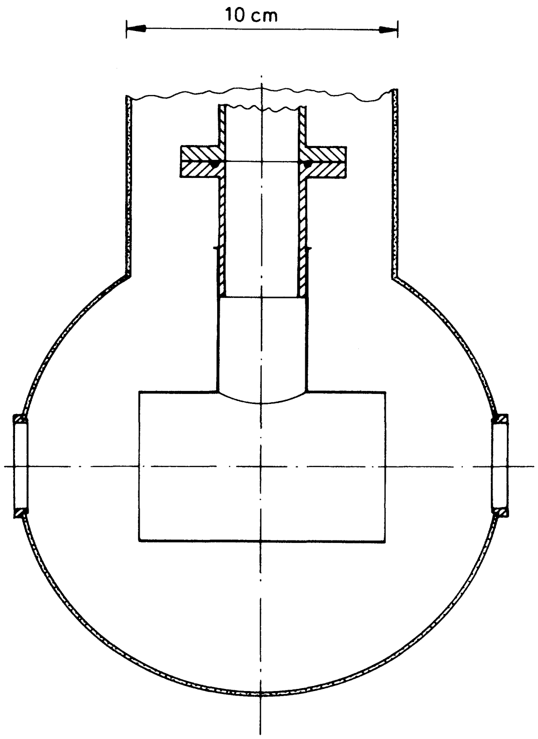

FIG. 1. Cross section through the vaccum vessel and the target cell for the liquid hydrogen. The cylindrical piece of the cell and the vessel's spherical part with extremly low mass density are shown. Two windows consisting of 20 μm Kapton foil are mounted for the primary particle beam.

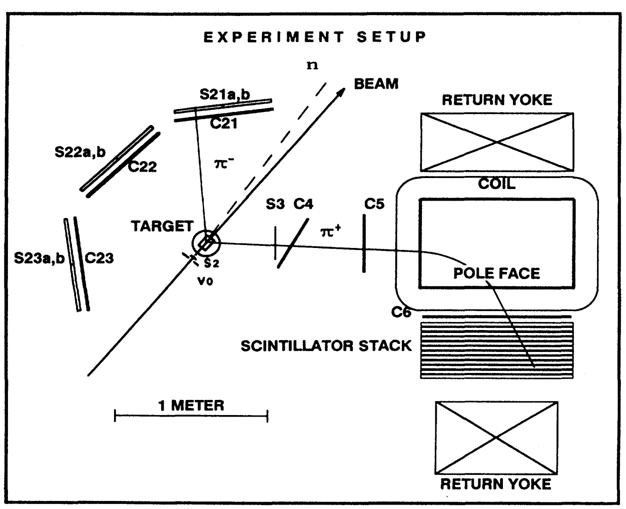

FIG. 2. Horizontal cross section through the apparatus. The incident pion beam is sketched together with the beam defining scintillators (V_0, S_2) and the target. The figure exhibits the tracks of a $(\pi, 2\pi)$ event. The π^+ is detected by the spectrometer (scintillator stack, scintillator S_3, and the MWPC's C_4, C_5, C_6). Out of the six panels for detecting the π^- only those intersecting the (x, z) plane are displayed.

C. Detectors

The main feature of the detection system was the combination of a magnetic spectrometer with its excellent particle selection possibilities together with rather simple detectors, covering a large solid angle. Figure 2 shows a horizontal cross section of the setup. After definition of the incident π^-, the produced π^+ was detected in the magnetic spectrometer, called the π^+ arm, whereas the π^- was observed in the so-called π^- arm.

1. Beam definition

The incident π^- beam was defined by an arrangement of the 1 mm thick scintillator S_2, 22 mm in diameter, and a veto scintillator V_0. This veto counter was a scintillator with a square active area of 20 cm $\times$ 20 cm and a central hole, 2 cm in diameter. The anticoincidence suppressed the muon halo of the beam to more than 90%. These two scintillators were mounted close together and were well adjusted 30 cm upstream from the target center. This distance was small enough with respect to the 3 mrad divergency of the focused beam to intersect only the center region of the target cell. Together with a signal from the intermediate hodoscope (H_1) and the radio frequency (ν_{RF}) of the cyclotron, the beam trigger (B_{trig}) was extracted electronically by

$$B_{\mathrm{trig}} = \overline{V}_0 S_2 \nu_{\mathrm{RF}} H_1 .$$

This provided a good separation of the π^- from the electrons in the beam. The S_2 signal, the hodoscope information, and the time of the ν_{RF} signal were recorded for each event. The remaining fraction of π^- in the beam was determined by evaluation of the timing of the beam-defining counter versus the radio frequency of the cyclotron. The μ^- contamination of the beam could also be decreased by more than 90% using the above mentioned time-of-flight spectrum. The remaining muon contribution of the beam not separated by TOF was estimated to be less than 1%. This was taken into account, where the errors of this correction itselves were estimated to be negligible.

2. The π^+ arm

As demonstrated in Sec. I D the identification of the π^+ is the essential trigger for the experiment. To ensure a very restrictive π^+ identification, a bending magnet was combined with a scintillator telescope. A standard beamline magnet was modified and supplied with MWPCs (C_4, C_5, C_6) and scintillators (S_3, scintillator stack) as shown in Fig. 2. The trigger scintillator S_3 is characterized by a thickness of 1 mm and an active area of 23.5 cm $\times$ 7.0 cm, read out by two photomultipliers. The chambers C_4 and C_5 at the entry of the magnet had a resolution of 2 mm in the horizontal and vertical directions. The chamber C_6 at the exit of the magnet had only vertical wires with 2 mm spacing. The polarity was selected by bending positive particles to the chamber C_6 and the range telescope. This delivered a strong primary selection of positive particles. The chambers fixed three points of the trajectory of the particle crossing the magnetic field. This trajectory could be reconstructed completely, using a well-known field map inside and outside of the dipole gap. Using the track information, the following observables for the π^+ were extracted: the direction of the produced π^+ eliminated the background reactions from non-hydrogen materials around the target; the tracklength was a necessary input to calculate the velocity of the particle; and the track shape delivered the particle momentum with a resolution of $\frac{\Delta p}{p} = 2.5\%$ (FWHM). Due to the absence of any quadrupole magnets, the distance of the center of the dipole to the target was only 1.90 m. This short distance enabled a high geometric aperture of 47 msr in combination with a sufficiently low pion decay rate. Figure 4 shows the acceptance (see Sec. II C 3) of more than 30 msr, which was simultaneously available for a very large momentum region (p = 80–300 MeV/c). These large values cause a moderate momentum resolution of $\frac{\Delta p}{p} = 2.5\%$ (FWHM), which is appropriate for this experiment.

This spectrometer was tested by elastically scattered π^+ produced on the LH_2 as well as on a carbon target. This was done in a momentum region of 110–350 MeV/c. The line shapes turned out to be nearly Gaussian.

The positive particles having traversed the magnet were stopped in a stack of 12 scintillator plates. The first plate is called S_4. Each plate consisted of NE102A material (Nuclear Enterprices) and was 1 m long, 24 cm high, and 2.5 cm thick. On the small surfaces, the light was coupled via adiabatic lightguides onto 7.6 cm photomultiplier tubes (Valvo XP2312B). In the momentum range selected by the magnet, protons stopped within the first two plates, pions within the 12 plates, while positrons sometimes traversed the whole stack.

The time and pulse height information from the scintillator stack was the source of the following: the time of flight (TOF), which was obtained with a resolution of 650 ps (FWHM); the kinetic energy of the stopped particles, given by the sum of all pulse height integrals; the range and dE/dx pattern for stopped particles; the π^+ decay cascade. It was observed by special electronics resolving double and triple pulses.

Altogether, the rich information of the complete π^+-arm detectors enabled the following: a strong separation of π^+ produced in the target; the determination of the quality (this means the efficiency of the π^+ identification and the background); and the determination of the momentum vector of the produced π^+.

The different independent identification methods allowed the efficiency calibration of each method. Overall, a pion identification efficiency of 72% with a simultaneous suppression of background reactions by 10^{-4} was achieved.

The complete spectrometer was placed at a distance of 1.90 m (to the center of the magnet) from the target under 50° towards the beam axis. The technical data of the spectrometer are listed in Table I.

TABLE I. Technical data of the π^+ spectrometer.

Weight	23t
Field gap: height	18 cm
Field gap: width	60 cm
Field gap: depth	100 cm
Used field	10 kG
Aperture	47 msr
Acceptance	> 30 msr at p = 80–300 MeV/c
Chamber resolution	2 mm
Scintillator stack	12 plates; $100 \times 24 \times 2.5$ cm^3 each
Typical total π^+ track length	215 cm

3. Spectrometer acceptance

In first approximation the acceptance of the spectrometer may be determined as a function of the π^+ momentum by ray-tracing Monte Carlo calculations. However, an estimation of the effect of multiple scattering, energy loss, and the pion decay showed the necessity of more detailed Monte Carlo calculations. These were done, including changes of the tracks, because of multiple elastic scattering according to Ref. [20] for small angles with an additional part with respect to elastic scattering to larger angles according to Ref. [21]. Pion decay and the energy loss of the pions were also included. The π^+ absorption and reactions in the traversed matter (target materials, MWPC's, air, etc.) was not included in these Monte Carlo calculations. Muons resulting from π^+ decay in the spectrometer were continued to be ray traced; however, they did not contribute to the acceptance. This is justified by the μ suppression of the apparatus as described in Sec. IV A. The ray tracing of these decay events was done only to get an estimation for the rate of "π^+ in flight decay" events, which could pass all cuts and tests of the data evaluation. Figure 3 shows the experimental line shape of the spectrometer in comparison to that of the Monte Carlo calculations. The position and width of the line is well reproduced by the calculations. The shape of the non-Gaussian tails is caused by the π scattering to larger angles and is also reproduced by the calculations. The Monte Carlo calculations underestimate the tails of the peak a little. The quite good agreement of both line shapes demonstrates the quality of our Monte Carlo calculations. Although this test was done at 170 MeV/c, it proves the validity of the acceptance calculations. The validity of our Monte Carlo acceptance curve is limited by π^+ absorption and inelastic scattering effects within the spectrometer, error propagation of the μ^+-suppression rate, and unknown π^+ elastic scattering cross sections for big angles. These effects were estimated and were considered to lead to an additional systematic error of the acceptance of ± 5% below 120 MeV/c and ± 10 % below 100 MeV/c.

Figure 4 shows the acceptance curve of the spectrometer as a result of the Monte Carlo calculations. The data points in this figure reflect experimental checks of this spectrometer efficiency by various methods.

In a momentum region of 110–350 MeV/c the spectrometer was tested by elastically scattered π^+ on a LH_2 as well as on a carbon target. A comparison with the cross sections from literature [22] showed the acceptance to be in good agreement with our Monte Carlo calculations. With respect to the possible beam normalization errors (at these low energies) and the errors of the literature values this is also true for the two points at about 110 MeV/c. Unfortunately, the πM1 beam line did not deliver π^+ with a momentum below 120 MeV/c at a reasonable rate.

To gain further information below 110 MeV/c, elastically scattered π^+ (from a carbon target) were degraded in front of the spectrometer by different materials. A momentum shift according to the expected values was observed together with a broadening of the lines. As far as the broadening of the lines allowed an observation no indication for abnormal line shapes was found. This was done down to 70 MeV/c. The degrader measurement led to the low energy acceptance value in Fig. 4. This value turned out to be far below the calculated curve. The systematic error of this value for the acceptance may be strongly enhanced by the poorly known absorption and straggling effects within the degrader at these low energies. The horizontal error bar in Fig. 4 at this point indicates the uncertainty in momentum, which was caused by the shift and broadening effects of the degrader.

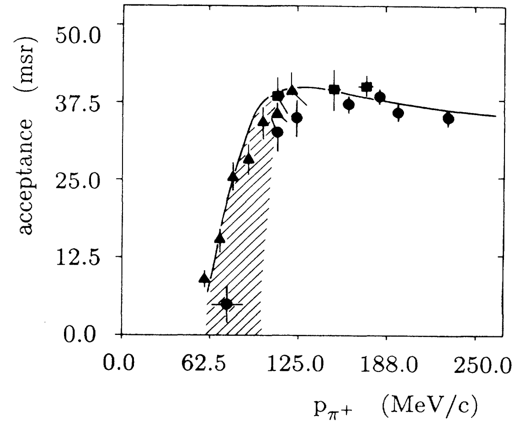

FIG. 4. Acceptance of the pion spectrometer versus the momentum. The solid line was determined by means of the Monte Carlo calculations. The hatched area indicates the problematic low energy region as mentioned in the text. The solid circles show experimental points produced by elastic π^+ scattering together with literature cross sections. For the low momentum point a degrader was used in front of the spectrometer. The squared points show the acceptance taken by a comparison with scintillator arrangements. The triangular points were produced using the wire chamber information.

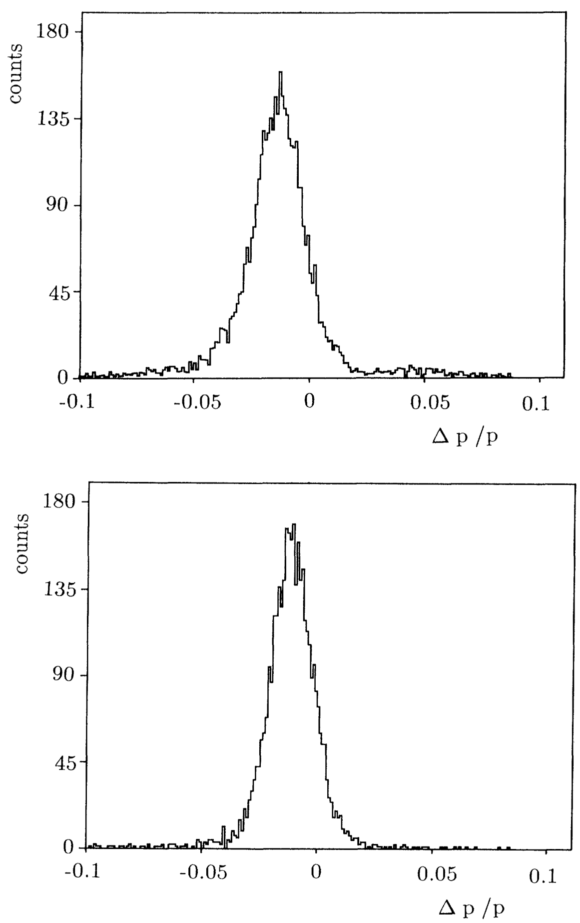

FIG. 3. Momentum resolution $\frac{\Delta p}{p}$ of the π^+ spectrometer at 170 MeV/c central momentum. (a) The spectrum was taken by elastic scattering on hydrogen. The kinematical momentum slope of the scattered pions has been considered in the calculation of p. (b) This momentum resolution was generated by the Monte Carlo calculations for similar conditions as (a).

To avoid these errors, we replaced the spectrometer by a simple scintillator arrangement. The flux of the π^+ after this elastic scattering and degrading process was accurately determined with this scintillator arrangement. The efficiency of a small scintillator telescope is better known than that of a magnetic spectrometer. The π^+ rate determined with this telescope was compared to that of the spectrometer. This resulted in acceptance values which were in better agreement ($\pm$ 10%) with the Monte Carlo curve. These acceptance points are indicated as squares in Fig. 4.

As a further check subsamples of pions very close to the central track of the spectrometer were prepared using the two wire chambers C_4 and C_5 in front of the spectrometer. This preparation was done for a well-known aperture at several magnetic settings. For this "incoming" central track we assumed a probability of 1 (without decay) for a pion to hit anywhere in the rear scintillator S_4. This assumption was checked to be true at 110 MeV/c by the use of an intermediate scintillator directly behind the MWPC C_5. Acceptance values were produced by comparing this pion rate with the total measured pion rate for the complete spectrometer. They reproduced the Monte Carlo curve within a scale of about 10% and 18% below 110 MeV/c, respectively. Although this method is not an absolute acceptance measurement, the good agreement with the Monte Carlo curve is astonishing. This is shown by the triangular points in Fig. 4.

This fact encouraged us to take the Monte Carlo calculation to determine the double differential cross section. It should be stressed that for the calculation of the more exclusive W function—the main observable of this experiment—knowledge of the acceptance is not necessary.

4. The π^- arm

As explained in Sec. I D, the knowledge of the direction of the outgoing π^- is necessary to determine the kinematics of the (π, 2π) events completely. To get this information, the outgoing π^- was detected in an array of low cost MWPCs combined with trigger scintillators. This part of the apparatus was segmented in 6 panels. Each panel consisted of a 64 cm × 64 cm active area MWPC with 1 cm wire spacing in two directions and two scintillation counters (32 × 64 × 2 cm^3, NE102A) behind the chamber. The panels were mounted at a distance of about 70 cm around the target to cover a sufficiently large angular region in polar as well as in azimuthal direction. The covered angular region is shown in Fig. 5. The symmetry of the $(\pi, 2\pi)$ events with respect to the (beam, π^+) plane, which is guaranteed by the parity conservation, simplified the positioning of the detectors. Especially the in-plane angles opposite to the spectrometer were covered from 15° to 160° by three panels. Since Fig. 2 is a cross section of the setup, only these three in-plane panels can be seen in it. The others were arranged out-of-plane to achieve a good information on the azimuthal angular distribution of the π^-. To provide insight into the probability of both pions going in nearly the same direction, some small scintillator counters (16 cm × 16 cm) were mounted additionally in the (beam, π^+) plane close to the spectrometer opening. Totally, a solid angle of 4 sr was covered by the π^- arm.

The panels delivered the π^- angles with a spacial resolution of 1°. The time resolution of the scintillators behind the chambers was 850 ps (FWHM). This value

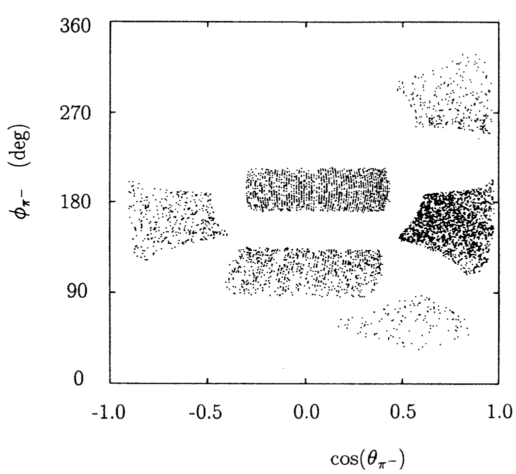

FIG. 5. Shown is a mapping of the second-arm panels in the $(\cos\theta_{\pi^-}, \phi_{\pi^-})_{\rm lab}$ plane. The dots refer to real coincident events seen in the second arm. Note that, due to the reaction kinematics, the distribution of events is symmetric to the $(\phi_{\pi^-} = 180°)$ axis.

was obtained by meantiming of the two phototube signals mounted on the opposite scintillator sides. The track information on the π^- was used to calculate the θ and ϕ angles of the π^- emission. This completed the kinematical set of variables for each $(\pi, 2\pi)$ event. Besides, the time of flight and pulse height information from the scintillators was used for kinematical checks.

D. Electronics

The trigger of the experiment was built up in several stages. The beam trigger $B_{\rm trig}$ (see Sec. II C 1) was combined with the condition that a particle traversed the spectrometer. This spectrometer trigger was achieved by the hit of the thin aperture scintillator S_3 and the pulses of both sides of the first scintillator plate S_4.

At this point, many elastically scattered protons passed this condition successfully. To achieve a better proton suppression a special feature of the spectrometer was used: despite the fact that protons of different momentum differ in time of flight through the spectrometer, proton signals of the phototube closer to the magnet entrance had nearly the same timing. This was due to the fact that the momentum of a fast proton caused the hit of the scintillator to be far away from this phototube. The long propagation time of the scintillation light to the phototube compensated for the short time of flight of the proton. This allowed a simple anticoincidence gate $G_{0\,\rm prot}$ to suppress 98% of the protons. An experimental comparison with and without this additional gate $G_{0\,\rm prot}$ showed no effect on the π^+ rate.

Furthermore, the pattern of hit plates in the scintillator stack was used. A good event must provide a continuous row $P_{\rm pat}$ of hit plates starting at the first plate. By this means, yoke scattering and area background of neutrons could be suppressed in the trigger. The pattern detection was done with a Memory Lookup Unit (Le Croy 2372).

The final hardware trigger built up by

$$T_{\rm trig} = B_{\rm trig} S_3 S_4 E_{G\,\rm prot} P_{\rm pat} \tag{2.1}$$

was used to start the readout of the component information. The low rate of $T_{\rm trig}$ events allowed taking the "free" π^+ events together with the coincident events. Except for the scintillator stack, all detectors were treated as usual. The scintillator pulses were led to ADC and TDC.

Typical particle rates for the π^- beam (depending on the production proton beam) were 1.2–2.4 MHz. At a rate for $B_{\rm trig}$ of 1.3 MHz we found 115 Hz for $B_{\rm trig}S_3$, 14 Hz for $B_{\rm trig}S_3S_4$, 2.6 Hz for $B_{\rm trig}S_3S_4G_{0\,\rm prot}$ and 2.5 Hz for $T_{\rm trig}$. The rate of coincident particles hitting the spectrometer and the second arm was 1 Hz of the 2.5 Hz $T_{\rm trig}$ events.

In particular, pulses of the scintillators in the range telescope were treated. To allow the search for signals of the pion decay, the analog pulse was cut into two pieces at its maximum [7,23]. Their charge integrals were taken separately by single gated ADCs (Le Croy 2249SG). The delayed decay (≥ 5 ns) of a stopped π^+ characteristically increased the second part of the pulse by about 4 MeV. This delivered a good pion signature.

III. COORDINATE SYSTEM AND FINAL OBSERVABLES

The coordinate system was chosen in the way that the incoming π^- beam is identical to the z axis. The outgoing π^+ defined the (x, z) plane. The y axis is perpendicular to the (x, z) plane defining a right-handed coordinate system. These coordinates are sketched in Fig. 6 together with the polar and the azimuthal angles θ and ϕ, respectively. In this coordinate system, the azimuthal angle of the π^+ is always zero by definition.

Excluding polarisation, the triple differential cross section $\frac{d^3\sigma}{d\Omega_{\pi^+} dT_{\pi^+} d\Omega_{\pi^-}}$ is the most exclusive observable for this three-body reaction. This triple differential cross section was obtained by the presented experiment:

$$\frac{d^3\sigma}{d\Omega_{\pi^+} dT_{\pi^+} d\Omega_{\pi^-}} = \frac{N_{\pi^+,\pi^-,T_{\pi^+}}}{N_{\rm tgt} N_B \epsilon_{\pi^+} \Delta\Omega_{\pi^+} \Delta T_{\pi^+} \epsilon_{\pi^-} \Delta\Omega_{\pi^-}}. \tag{3.1}$$

$N_{\pi^+,\pi^-,T_{\pi^+}}$ denotes the number of events, where the π^+ within a kinetic energy range ΔT_{π^+} and the outgoing π^- were identified coincidently; $N_{\rm tgt}$ denotes the density of hydrogen atoms per unit area in the target; ϵ_{π^+} denotes the detection and identification efficiency for positive pions in the spectrometer; $\Delta\Omega_{\pi^+}$ denotes the solid angle of the π^+, covered by the spectrometer; ΔT_{π^+} denotes the energy interval for the detected π^+; N_B denotes the number of π^- in the beam hitting the target; ϵ_{π^-} denotes the detection and identification efficiency for negative pions in the π^- arm; and $\Delta\Omega_{\pi^-}$ denotes the considered solid angle of the π^- arm.

A less exclusive observable is the double differential cross section $\frac{d^2\sigma}{d\Omega_{\pi^+} dT_{\pi^+}}$. Some data for this quantity in this energy region are given in Refs. [7, 10–12]. This double differential cross section may be derived from the triple differential cross section by integration over all π^- emission angles. This means the measuring of the free π^+ production coming from the reaction $\pi^- p \to \pi^+\pi^- n$ without observing the π^-.

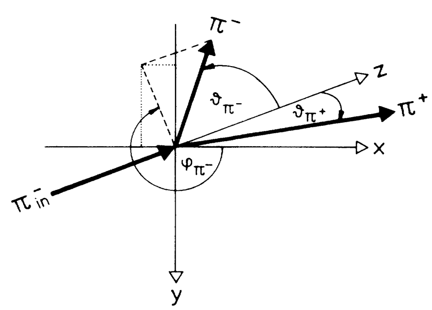

FIG. 6. Coordinate system of the experiment, defined by the incoming beam in the z direction and the outgoing π^+ in the (x, z) plane. The polar angle is defined with respect to the z axis, the azimuthal angle is defined to be zero in the (x, z) plane.

It is given by

$$\frac{d^2\sigma}{d\Omega_{\pi^+} dT_{\pi^+}} = \frac{N_{\pi^+,T_{\pi^+}}}{N_{\rm tgt} N_B \epsilon_{\pi^+} \Delta\Omega_{\pi^+} \Delta T_{\pi^+}}, \tag{3.2}$$

where $N_{\pi^+,T_{\pi^+}}$ denotes the number of detected π^+ from the $(\pi, 2\pi)$ reaction within the range of the kinetic energy given by ΔT_{π^+} (all other definitions as above).

The double and triple differential cross sections depend in the same way on several experimental uncertainties (like target thickness, spectrometer acceptance, etc.). Therefore, the normalization of the triple differential cross section to the double differential cross section provides the elimination of most of these systematic error sources, but still yields the angular shape of the triple differential cross section. This leads to the angular correlation function

$$W(\phi_{\pi^-}, \theta_{\pi^-}) = 4\pi \frac{\frac{d^3\sigma}{d\Omega_{\pi^+} dT_{\pi^+} d\Omega_{\pi^-}}}{\frac{d^2\sigma}{d\Omega_{\pi^+} dT_{\pi^+}}}. \tag{3.3}$$

The normalization factor 4π gives $W \equiv 1$ for isotropic emission of the π^-. W reflects the emission probability of a π^- in the $(\theta_{\pi^-}, \phi_{\pi^-})$ space, when a reaction of the $(\pi, 2\pi)$ type with defined π^+ angle and energy occurred. Combining Eqs. (3.1), (3.2), and (3.3), the experimental uncertainties according to target thickness, the size, and shape of the spectrometer acceptance and incoming pion flux cancel:

$$W(\Delta\Omega_{\pi^+}, \Delta T_{\pi^+}, \Delta\Omega_{\pi^-}) = 4\pi \frac{N_{\pi^+,\pi^-,T_{\pi^+}}}{N_{\pi^+,T_{\pi^+}} \Delta\Omega_{\pi^-} \epsilon_{\pi^-}}. \tag{3.4}$$

Being free of the most severe systematic errors, this observable allows a refined analysis of the dynamics of the $(\pi, 2\pi)$ reaction.

The angular correlation function W was the main observable of the experiment. In addition, the double differential cross section was measured. In contrast to the W function, it was affected by the usual systematic error sources leading to a normalization error of $\pm 14\%$.

Of course, the triple differential cross section can be calculated reversely from our data by

$$\frac{d^3\sigma}{d\Omega_{\pi^+} dT_{\pi^+} d\Omega_{\pi^-}} = \frac{W}{4\pi} \frac{d^2\sigma}{d\Omega_{\pi^+} dT_{\pi^+}} \tag{3.5}$$

importing the overall uncertainty of $\frac{d^2\sigma}{d\Omega_{\pi^+} dT_{\pi^+}}$.

IV. OFF-LINE ANALYSIS

In this section, the process of event classification and identification of the π^+ in the spectrometer and the π^- in the so-called second arm will be described. Furthermore, the extraction of the W-function data and cross section data from the sample of identified $(\pi, 2\pi)$-events is presented.

As stated in Sec. I, the π^+ identification is the crucial point of this experiment. In principle, the spectrometer dipole magnet selected the positive charged particles coming from the target. Fortunately, in this energy region only a few reactions can produce such a positive particle using a beam of negative pions. These positive particles are the following: positrons (e^+), produced mainly by $\pi^- p \to \pi^0 n$ and $\pi^0 \to e^+ e^- \gamma$; protons (p) from $\pi^- p \to \pi^- p$ and $\pi^- p \to \pi^- \pi^0 p$; light ions, produced by reactions from background materials other than hydrogen; pions (π^+) from $\pi^- p \to \pi^+ \pi^- n$ and $\pi^- X \to \pi^+ Y$ (occurs in non-hydrogen materials via DCX); and muons (μ^+) from the decay of π^+.

These mechanisms are expected to be the dominating processes, which produced events in our apparatus. Of course, one can think of more complicated mechanisms based on double scattering within the target, electromagnetic and weak interactions. All of these mechanisms are estimated to be many orders of magnitude lower than the $(\pi, 2\pi)$ reaction.

Therefore, the events with positive pions triggering the spectrometer arm of the experiment had to be separated from the above-mentioned background events.

For the further data interpretation two types of events were distinguished: events with a π^+ emission into the spectrometer from the $(\pi, 2\pi)$ reaction without regard to the π^- detection, leading to $\frac{d^2\sigma}{d\Omega dT}$ ["free $(\pi, 2\pi)$ events"]; events with a π^+ emission into the spectrometer and the detection of the corresponding π^- from the $(\pi, 2\pi)$ reaction, leading to the W function ["complete $(\pi, 2\pi)$ events"].

Therefore, the data analysis was a two-step process. First, the events with a π^+ emission into the spectrometer were filtered. In a second step, the coincident π^- was identified. All events, which passed the first step of the evaluation are the so-called "free $(\pi, 2\pi)$ events." The events with the coincident π^- are called "complete $(\pi, 2\pi)$ events."

A. π^+ identification

As pointed out in Sec. II C 2 the momentum p and the track length of the positive particle were processed for each event by using the chamber hit information of the spectrometer. This was performed by an analytic formula, whose parameters were fitted to ray-tracing calculations based on the measured field map. The quality of the method was tested by low energy elastic π^+ scattering: the momentum resolution proved to be $\frac{\Delta p}{p} < 2.5\%$ (FWHM). The track data of the positive particles were supplemented by the time of flight and pulse height information derived from the scintillator stack. This led to the calculation of physically relevant quantities.

The velocity v from the track length in the spectrometer and the time of flight (TOF). Using the velocity v and the momentum p, the mass of the particle can be calculated as

$$m_1 := \frac{p}{v}\sqrt{1 - \frac{v^2}{c^2}}. \tag{4.1}$$

Figure 7(a) shows the typical structure of the m_1 spectrum of the detected particles. It consists of a big bump of protons at the high end of the mass scale, a diffuse heap of positrons on the low end of the scale and a sharp pion peak with a shoulder of muons on its low mass side. Because the value of the time of flight information rises with decreasing particle energy, the particle mass calculation from time of flight and momentum succeeds better for low energetic pions and muons. This leads to the positive effect, which especially at low energies where pion decay in the spectrometer is more likely, the muons from the pion decay could be separated quite well.

Another access to the particle mass was possible by combining the kinetic energy (E_k) of stopped particles and the momentum. The kinetic energy of the particle was evaluated by the sum of the ADC information of the scintillator stack.

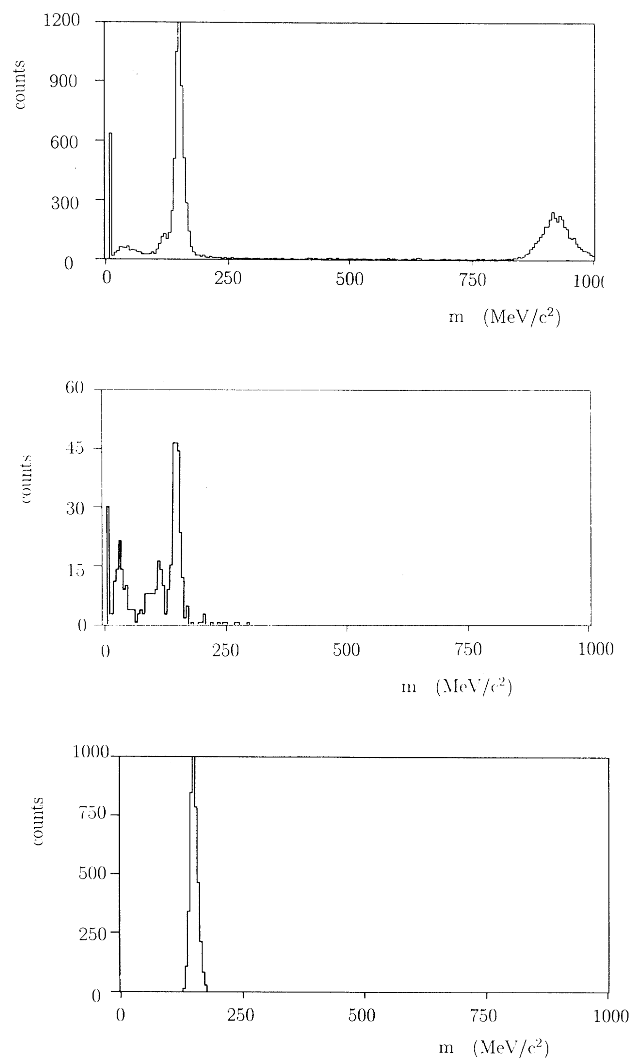

FIG. 7. Distribution of particle mass taken by the spectrometer via time of flight and momentum. Electrons and protons are already suppressed by hardware trigger. (a) Distribution for one run of taped events with an unique track information in the spectrometer. (b) Same as (a), with the additional request on the momentum to be lower than 80 MeV/c. The π and μ peak separate for lower momenta. (c) Same as (a), with true software trigger as described in Eqs. (4.3) and (4.4).

$$m_2 := \frac{1}{c^2}\left(\frac{p^2c^2 - E_k^2}{2E_k}\right). \tag{4.2}$$

The distribution of this value also shows a well-defined pion peak. Figure 8 shows the typical structure of the m_2 spectrum integrated over all observed momenta. The mass resolution is rising with decreasing particle momentum. However, this pion peak is located on a broad, widely spread background of the electron component. This background was due to the fact that in general the electron deposed not all energy in the scintillator stack (emission of bremsstrahlung). The particle was assumed to be a pion, if the value m_2 was within an interval m_π (1 ± 0.1). For these events the value M_2 was set to T_{true}.

Furthermore, some qualitative signatures of the π^+, which are independent of the mass calculations, could be derived for the identification:

The occurrence of the typical π^+ decay cascade. As described in Sec. II D, the photomultiplier signals of the scintillator stack were cut at their maximum into two pieces by electronics. This maximum occurred 5 ns after the start of the pulse. The long part signal was defined by a 60 ns gate. The charge contents of the two pieces were plotted versus each other. For signals without decay the two pieces are proportional to each other and the resulting plot shows a linear behavior. In case of stopped π^+, the second part will be increased by an additional signal from the 4.1 MeV μ^+ produced by the $\pi^+ \to \mu^+ + \nu_\mu$ decay. This led to a shift of the line with respect to the above-mentioned one. The two lines were clearly separated due to the energy resolution of 10% for a signal up to 25 MeV from a π^+ stopped in one scintillator plate. For all events detected in the shifted line the variable D_π was set to T_{true}.

The μ-decay track. Due to the low range of the 4.1 MeV μ^+ in matter, the μ^+ decayed in the same or a neighbored scintillator plate, where the muon production occurred. The positron from the decay $\mu^+ \to e^+ + \nu_e + \bar{\nu_\mu}$ may be observed several microseconds after the pion decay. This decay caused a continuous track starting at the stopping plate (or one beneath). This event was searched for a period of 10 μs with a timesliced pattern unit. The detection of this signature resulted in the variable $D_\mu = T_{\text{true}}$. This method separated protons and positrons from pions and muons. The method was applicable because of the low particle rate in the spectrometer.

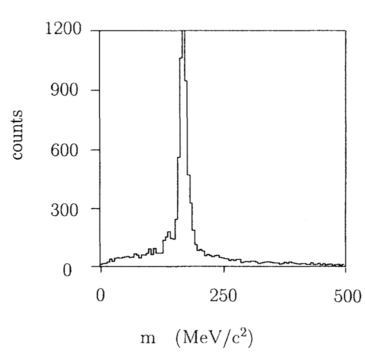

FIG. 8. Distribution of particle mass taken by the spectrometer via measured kinetic energy and momentum.

The specific energy loss in scintillator material. The different particle types stopped in the scintillator stack cause a characteristic energy loss distribution in the plates of the scintillator stack. The characteristics became most evident in the last two hit plates. By comparison of these two signals, the different particle types could be distinguished; in particular, protons and electrons were separated quite well. The muons behaved rather similar to pions. Therefore, they could not be well discriminated from the pions by this method. All events which showed a pionlike behavior were marked with $E_{\text{loss}} = T_{\text{true}}$.

The m_1 spectrum allowed a clear distinction (Fig. 7) between the different particles. Therefore, it was suitable for calibration of the different π^+ identification methods. The combination of these more or less independent identification methods turned out to be a powerful tool for background suppression. This could be clearly observed in the m_1 spectrum. The π^+-identification efficiencies of the different combinations were determined by their effect on the m_1 spectrum. Various m_1 spectra resulting from events fulfilling different identification methods were generated. The fraction of the π^+ was obtained by fitting these m_1 spectra assuming Gaussian distributions. The ratio of the integrals for each particle mass region to the integrals of the original (free) spectra gave the identification rate.

The following combination showed a good π^+-identification rate combined with a high rejection rate for e^+ and p in the m_1 spectrum:

$$T_{\text{trig}} = D_\pi + E_{\text{loss}} M_2 + E_{\text{loss}} D_\mu \tag{4.3}$$
$$(+ : \text{"OR"}; \cdot : \text{"AND"}).$$

For these particles that hit only one or two scintillator plates of the scintillator stack (especially low energetic muons and protons) the E_{loss} cut was not possible. In this case the trigger was chosen to be

$$T_{\text{trig}} = D_\pi + M_2 D_\mu . \tag{4.4}$$

Together with the m_1 spectrum this rather complicated trigger allowed even the separation of overlapping muons and pions in most of the cases: Muons from pion decay in front of the spectrometer and between the chamber C_4 and C_5 are rejected because their tracks do not intersect the target. Muons from pion decay within the magnetic field show a nearly unchanged time of flight, but in general the direction of the track is changed due to the decay and thus also to the observed momentum. Therefore they were separated in the m_1 spectrum. For the low energy pions the fraction of the pion decay events is low due to the short track length of about 40–80 cm within the magnetic field. For lower momenta, where the pion decay is more likely, the muons could not pass more than 2 scintillator plates. This led to the more restrictive trigger 4.4. On the other hand, the muon separation via time of flight succeeds better at lower energies as shown in Fig. 7(b).

The excellent background suppression of the trigger is demonstated in Fig. 7(c) containing only the π^+ peak. Of course there is a fraction of μ^+ from π^+ decay which could pass the tests because they leave track direction and observed momentum data unchanged with respect to a possible π^+ track. The rate has been estimated by Monte Carlo calculations to be below 2.5% within 50–100 MeV/c. Since these muons originate certainly also from $\pi^- p \rightarrow \pi^+\pi^- n$ events and leave the kinematical observables unchanged, they do not lead to a background. Their rate was taken into account for the calculation of the double differential cross section.

As mentioned above, for particles coming from the target region the method resulted in an overall π^+ identification of 72% with a simultaneous suppression of the background particles by 10^{-4}.

B. π^- coincidence

After the π^+ detection, a simultaneously ejected second particle was sought. One of the large area scintillators of the second arm was expected to be hit in a certain time window. This time window was defined by the condition that the particle velocity was between $\beta = 1$ and $\beta = 0.3$. This was calibrated by elastic scattering. In the case of a chamberhit in front of the triggering, corresponding scintillator, the particle was assumed to be charged. The chambers of the second arm delivered the angle and the exact distance of the hit to the target, assuming that the particle track origin was the target. This was checked to be true in most of the cases by a special test described in Sec. IV D. Using the information of the corresponding π^+ in the spectrometer in addition to the emission angles of the second arm particle, the $(\pi,\ 2\pi)$ kinematics of the event was calculated. This delivered a prediction for the velocity of the supposed π^-. The good time-of-flight resolution in the second arm allowed a comparison of this predicted value to the measured velocity. The reference was calibrated by the use of elastic scattering. The resulting plot of the time-of-flight difference between calculation and measurement versus the energy loss in the scintillator is shown in Fig. 9. The energy loss

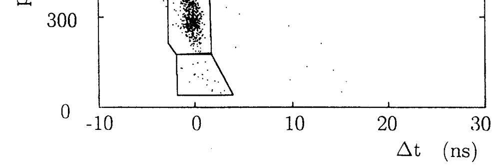

FIG. 9. Difference of the measured and the kinematically determined π^- time of flight versus the energy loss in the scintillator. The energy loss is given by the pulse height in the scintillator.

was given by the pulse height in the scintillation counter.

In this plot, the pions from the $(\pi,\ 2\pi)$ reaction could be separated from some other particles by using the drawn boxes in Fig. 9. The background of reactions not matching the $(\pi,\ 2\pi)$ kinematics in this procedure was lower than 1%. The bunch of particles at low energy loss, which is shifted towards bigger time difference, results from the leading-edge triggering of the discriminators. This identification method was applied to each element of the second arm in the same way. The events fulfilling this test were taken as "complete $(\pi,\ 2\pi)$ events."

C. Extraction of the physical observables

1. The angular correlation function W

To extract physical observables the selected nearly pure $(\pi, 2\pi)$ sample had to be normalized to solid angles, momentum regions, etc. Like every low energy $(\pi, 2\pi)$ experiment the one presented here suffers from the fact that parts of the phase space are unobservable, because of the low energy of the final states. This had to be considered when the efficiencies and detection probabilities of the various components of the experiment were determined.

The angular correlation function W is defined in Sec. III. It connects the double differential cross section $\frac{d^2\sigma}{d\Omega_{\pi^+} dT_{\pi^+}}$ with the triple differential cross section $\frac{d^3\sigma}{d\Omega_{\pi^+} dT_{\pi^+} d\Omega_{\pi^-}}$. With respect to experimentally obtained observables, W behaves like

$$W(\Delta\Omega_{\pi^+}, \Delta T_{\pi^+}, \Delta\Omega_{\pi^-}) = 4\pi \frac{N_{\pi^+,\pi^-,T_{\pi^+}}}{N_{\pi^+,T_{\pi^+}} \Delta\Omega_{\pi^-} \epsilon_{\pi^-}} \tag{4.5}$$

The total data set of 91 000 "free" $(\pi,\ 2\pi)$ events contained 32 000 "complete" $(\pi, 2\pi)$ events. These events were grouped into intervals according to their particular kinematics. In a first step the sample of "complete" $(\pi, 2\pi)$ events was distributed into six samples with different momenta of the π^+ in the laboratory system. The chosen momentum intervals are listed in Table II. Due

TABLE II. Momentum regions for the π^+ in the laboratory and the c.m. system, respectively. They are chosen as classification criteria for the presentation of the angular correlation data W (see Tables III–XLIV). The overlap of the $p^{\text{c.m.}}$ ranges is due to the kinematical transformations applied to the finite π^+ angular range. There is no double counting of $\pi^- p \rightarrow \pi^+\pi^- n$ events in the six momentum regions.

$p_{\min}^{\text{lab}}$ [MeV/c]	$p_{\max}^{\text{lab}}$ [MeV/c]	$p_{\min}^{\text{c.m.}}$ [MeV/c]	$p_{\max}^{\text{c.m.}}$ [MeV/c]
50	102	37	84
102	117	75	97
117	132	89	111
132	147	102	124
147	162	116	138
162	200	129	174

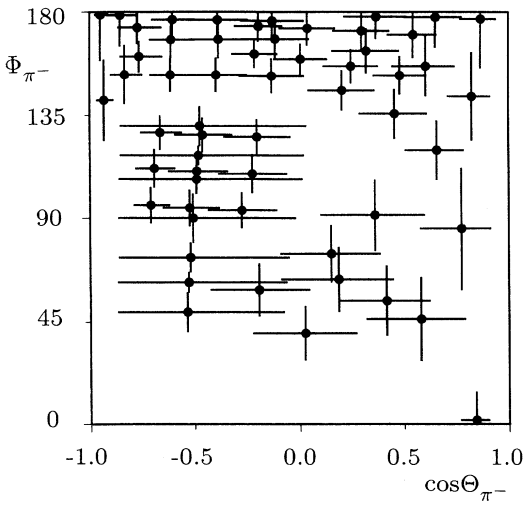

FIG. 10. Map of the W-function data points for one momentum interval. The size of the bars is given by the partition of the total solid angle. All data points for the first momentum region are plotted in the ($\cos\theta_{\pi^-}$, ϕ_{π^-}) space (c.m. system).

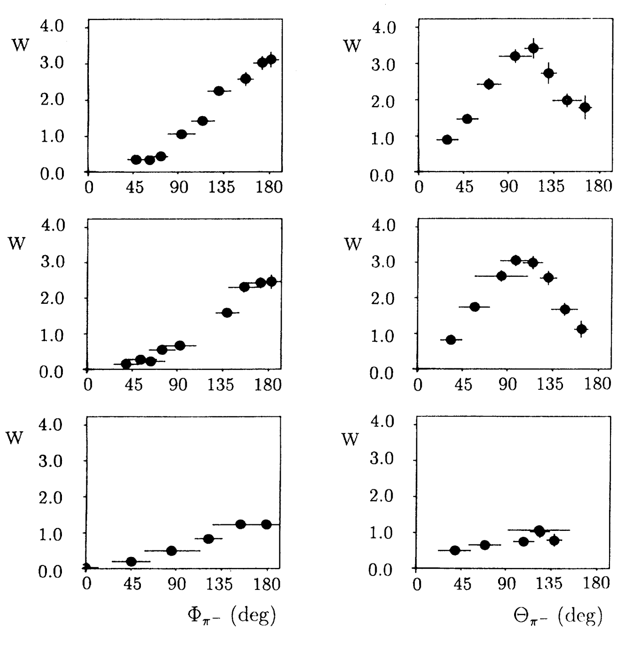

FIG. 11. Left side: angular correlation function W as a function of ϕ_{π^-} for various polar angles (corresponding to Tables XXXI, XXXIII, and XXXIV top to bottom) of the π^-. Right side: angular correlation function W as a function of θ_{π^-} for various azimuthal angles (corresponding to Tables XXXV, XXXVI, and XXXVII top to bottom) of the π^-. The other kinematical variables have been fixed to $p_{\pi^+} =$ 127 MeV/$c \pm$ 11 MeV/c and $\theta_{\pi^+} = 69° \pm 10°$ at an incoming energy of 284 MeV.

TABLE III. Angular correlation function W for different angles of the π^-. The corresponding π^+ momentum is $p_{\pi^+}^{\text{c.m.}} \in$ [37 MeV/c; 84 MeV/c], $\theta_{\pi^+}^{\text{c.m.}} = 91° \pm 10°$. The angles are given in degrees.

$\theta_{\pi^-}^{\text{c.m.}}$	$\phi_{\pi^-}^{\text{c.m.}}$	W	ΔW
114	176	2.805	0.205
114	168	2.263	0.172
114	152	2.424	0.187
115	128	2.223	0.123
115	111	1.574	0.095
112	92	0.920	0.080
112	72	0.607	0.100
112	62	0.388	0.097
112	49	0.370	0.068

to the fact that the laboraotry angle of the π^+ was fixed to 50° $\pm$ 10° by the aperture of the spectrometer, an unique transformation of the momentum regions into the c.m. system is possible. Furthermore, each of these six subsamples was treated individually. The next division into segments was done in laboratory ($\theta_{\pi^-}^{\text{lab}}$, $\phi_{\pi^-}^{\text{lab}}$) space. The limits were chosen to be along the chamber wires. This allowed a well-defined sorting. In general, the division of the observed π^- solid angle was done in pieces of about 21 cm $\times$ 21 cm in a distance of 80 cm from the target (approximately 0.07 sr). The sizes of these subsamples were compared with Monte Carlo calculations. These Monte Carlo events were created assuming a homogenous distribution in phase space and transformed into the laboratory system. To the Monte Carlo sample, the same division system as for the real events was applied. In addition, the special features of our apparatus were taken into account for the Monte Carlo events. These were a minimal momentum for the outgoing π^- of 50 MeV/c (this limit was estimated by energy loss and range calculations); the individual chamber efficiencies ϵ_{π^-} were determined by elastic scattering. With regard to a possible energy dependence of the chamber efficiency, the energy of the incident beam was varied. For lower energies the chamber efficiencies were calculated from the $(\pi, 2\pi)$ events themselves. In detail, a very strict cut was made with $(\pi, 2\pi)$ events demanding a time of flight near the kinematically fixed value and pulse height signals in the second arm. This delivered a database of low energy

TABLE IV. Angular correlation function W for different angles of the π^-. The corresponding π^+ momentum is $p_{\pi^+}^{\text{c.m.}} \in$ [37 MeV/c; 84 MeV/c], $\theta_{\pi^+}^{\text{c.m.}} = 91° \pm 10°$. The angles are given in degrees.

$\theta_{\pi^-}^{\text{c.m.}}$	$\phi_{\pi^-}^{\text{c.m.}}$	W	ΔW
90	174	2.389	0.170
90	160	2.589	0.145
94	125	2.464	0.246
95	109	1.246	0.159
97	93	0.873	0.139
90	58	0.332	0.065

TABLE V. Angular correlation function W for different angles of the π^-. The corresponding π^+ momentum is $p_{\pi^+}^{\text{c.m.}} \in$ [37 MeV/c; 84 MeV/c], $\theta_{\pi^+}^{\text{c.m.}} = 91° \pm 10°$. The angles are given in degrees.

$\theta_{\pi^-}^{\text{c.m.}}$	$\phi_{\pi^-}^{\text{c.m.}}$	W	ΔW
63	177	2.581	0.216
67	167	2.247	0.157
66	151	1.845	0.135
57	135	1.221	0.134
61	91	0.606	0.068
72	74	0.511	0.079
69	63	0.288	0.048
57	54	0.281	0.059
77	40	0.100	0.035

pions traversing the chambers and covering the scintillators. The energy dependence of the chamber efficiencies turned out to be a minor effect of 2–3%.

The angular correlation function W was calculated by

$$W = \frac{N^{\text{meas}}_{\pi^+,\pi^-,T_{\pi^+}}}{N^{\text{meas}}_{\pi^+,T_{\pi^+}}} \Bigg/ \frac{N^{\text{MC}}_{\pi^+,\pi^-,T_{\pi^+}}}{N^{\text{MC}}_{\pi^+,T_{\pi^+}}} \tag{4.6}$$

where $N^{\text{meas}}_{\pi^+,\pi^-,T_{\pi^+}}$ is the number of measured "complete" $(\pi, 2\pi)$ events, $N^{\text{meas}}_{\pi^+,T_{\pi^+}}$ is the number of measured "free" $(\pi, 2\pi)$ events, $N^{\text{meas}}_{\pi^+,\pi^-,T_{\pi^+}}$ is the number of Monte Carlo "complete" $(\pi, 2\pi)$ events, and $N^{\text{meas}}_{\pi^+,T_{\pi^+}}$ is the number of Monte Carlo "free" $(\pi, 2\pi)$ events.

This angular correlation data points depend on the four kinematical values $\theta_{\pi^+}^{\text{lab}}$, $\phi_{\pi^+}^{\text{lab}}$, $\theta_{\pi^-}^{\text{lab}}$, $\phi_{\pi^-}^{\text{lab}}$ according to the way of the chosen sorting system of the events. Since these four values build (together with the momentum of the π^+) a kinematically complete set of parameters, the momentum-energy vector can easily be transformed to the c.m. system. As a Lorentz scalar, W is invariant under this transformation. This led to a list of W data in the c.m. system. Figure 10 shows the position of the W values for the π^+ momentum range ($147.5 < p_{\pi^+}^{\text{lab}} < 162.5$ MeV/c, $40° < \theta_{\pi^+}^{\text{lab}} < 60°$) in the $(\theta_{\pi^-}, \phi_{\pi^-})$ plane. The symmetry of the reaction mechanism under reflection on the (x, z) plane (due to parity conservation) is used in this figure. The size of the crosses indicate the size of the corresponding detection elements. Intersecting areas were obtained during different beam times. Values of the

TABLE VI. Angular correlation function W for different angles of the π^-. The corresponding π^+ momentum is $p_{\pi^+}^{\text{c.m.}} \in$[37 MeV/$c$; 84 MeV/$c$], $\theta_{\pi^+}^{\text{c.m.}} = 91° \pm 10°$. The angles are given in degrees.

$\theta_{\pi^-}^{\text{c.m.}}$	$\phi_{\pi^-}^{\text{c.m.}}$	W	ΔW
41	174	1.118	0.082
40	149	1.332	0.093
44	119	0.949	0.119
34	85	0.619	0.067
47	46	0.307	0.048
28	1	0.035	0.100

TABLE VII. Angular correlation function W for different angles of the π^-. The corresponding π^+ momentum is $p_{\pi^+}^{\text{c.m.}} \in$ [37 MeV/c; 84 MeV/c], $\theta_{\pi^+}^{\text{c.m.}} = 91° \pm 10°$. The angles are given in degrees.

$\theta_{\pi^-}^{\text{c.m.}}$	$\phi_{\pi^-}^{\text{c.m.}}$	W	ΔW
155	174	2.030	0.197
139	175	2.369	0.184
121	176	2.658	0.301
107	176	2.922	0.280
90	174	2.389	0.170
65	174	2.564	0.175
45	177	1.329	0.139
27	176	0.844	0.111

TABLE VIII. Angular correlation function W for different angles of the π^-. The corresponding π^+ momentum is $p_{\pi^+}^{\text{c.m.}} \in$ [37 MeV/c; 84 MeV/c], $\theta_{\pi^+}^{\text{c.m.}} = 91° \pm 10°$. The angles are given in degrees.

$\theta_{\pi^-}^{\text{c.m.}}$	$\phi_{\pi^-}^{\text{c.m.}}$	W	ΔW
153	148	2.199	0.207
137	156	2.908	0.211
121	160	2.281	0.190
107	160	2.384	0.169
90	160	2.589	0.145
77	164	2.137	0.143
52	154	1.489	0.122
31	143	1.138	0.122

TABLE IX. Angular correlation function W for different angles of the π^-. The corresponding π^+ momentum is $p_{\pi^+}^{\text{c.m.}} \in$ [37 MeV/c; 84 MeV/c], $\theta_{\pi^+}^{\text{c.m.}} = 91° \pm 10°$. The angles are given in degrees.

$\theta_{\pi^-}^{\text{c.m.}}$	$\phi_{\pi^-}^{\text{c.m.}}$	W	ΔW
127	95	1.190	0.206
112	94	0.855	0.144
112	90	0.947	0.097
97	93	0.873	0.139
61	91	0.606	0.068
34	85	0.619	0.067

TABLE X. Angular correlation function W for different angles of the π^-. The corresponding π^+ momentum is $p_{\pi^+}^{\text{c.m.}} \in$ [75 MeV/c; 97 MeV/c], $\theta_{\pi^+}^{\text{c.m.}} = 76° \pm 10°$. The angles are given in degrees.

$\theta_{\pi^-}^{\text{c.m.}}$	$\phi_{\pi^-}^{\text{c.m.}}$	W	ΔW
114	176	3.016	0.200
115	168	2.344	0.164
115	152	2.443	0.176
116	128	2.127	0.117
116	111	1.613	0.095
113	92	0.941	0.081
114	72	0.522	0.094
114	62	0.674	0.130
114	49	0.469	0.077

TABLE XI. Angular correlation function W for different angles of the π^-. The corresponding π^+ momentum is $p_{\pi^+}^{\text{c.m.}} \in$ [75 MeV/c; 97 MeV/c], $\theta_{\pi^+}^{\text{c.m.}} = 76° \pm 10°$. The angles are given in degrees.

$\theta_{\pi^-}^{\text{c.m.}}$	$\phi_{\pi^-}^{\text{c.m.}}$	W	ΔW
90	174	3.112	0.188
91	160	2.539	0.136
95	125	2.082	0.211
96	109	1.632	0.171
98	93	0.959	0.136
91	58	0.309	0.059

TABLE XII. Angular correlation function W for different angles of the π^-. The corresponding π^+ momentum is $p_{\pi^+}^{\text{c.m.}} \in$ [75 MeV/c; 97 MeV/c], $\theta_{\pi^+}^{\text{c.m.}} = 76° \pm 10°$. The angles are given in degrees.

$\theta_{\pi^-}^{\text{c.m.}}$	$\phi_{\pi^-}^{\text{c.m.}}$	W	ΔW
64	177	2.380	0.193
67	167	2.128	0.145
67	151	1.859	0.130
58	135	1.726	0.148
62	91	0.498	0.057
74	74	0.339	0.059
71	63	0.324	0.047
58	54	0.205	0.046
79	40	0.139	0.039

TABLE XIII. Angular correlation function W for different angles of the π^-. The corresponding π^+ momentum is $p_{\pi^+}^{\text{c.m.}} \in$ [75 MeV/c; 97 MeV/c], $\theta_{\pi^+}^{\text{c.m.}} = 76° \pm 10°$. The angles are given in degrees.

$\theta_{\pi^-}^{\text{c.m.}}$	$\phi_{\pi^-}^{\text{c.m.}}$	W	ΔW
42	174	1.358	0.084
40	149	1.170	0.080
45	119	0.780	0.099
35	85	0.506	0.056
48	46	0.194	0.035
28	1	0.033	0.100

TABLE XIV. Angular correlation function W for different angles of the π^-. The corresponding π^+ momentum is $p_{\pi^+}^{\text{c.m.}} \in$ [75 MeV/c; 97 MeV/c], $\theta_{\pi^+}^{\text{c.m.}} = 76° \pm 10°$. The angles are given in degrees.

$\theta_{\pi^-}^{\text{c.m.}}$	$\phi_{\pi^-}^{\text{c.m.}}$	W	ΔW
156	174	2.358	0.208
140	175	2.873	0.197
122	176	3.697	0.338
107	176	2.505	0.241
90	174	3.112	0.188
66	174	2.307	0.158
46	177	1.500	0.136
27	176	1.048	0.114

TABLE XV. Angular correlation function W for different angles of the π^-. The corresponding π^+ momentum is $p_{\pi^+}^{\text{c.m.}} \in$ [75 MeV/c; 97 MeV/c], $\theta_{\pi^+}^{\text{c.m.}} = 76° \pm 10°$. The angles are given in degrees.

$\theta_{\pi^-}^{\text{c.m.}}$	$\phi_{\pi^-}^{\text{c.m.}}$	W	ΔW
153	148	2.363	0.210
138	156	2.496	0.189
122	160	2.414	0.184
107	160	2.374	0.158
91	160	2.539	0.136
78	164	2.050	0.134
53	154	1.406	0.111
31	143	0.847	0.096

TABLE XVI. Angular correlation function W for different angles of the π^-. The corresponding π^+ momentum is $p_{\pi^+}^{\text{c.m.}} \in$ [75 MeV/c; 97 MeV/c], $\theta_{\pi^+}^{\text{c.m.}} = 76° \pm 10°$. The angles are given in degrees.

$\theta_{\pi^-}^{\text{c.m.}}$	$\phi_{\pi^-}^{\text{c.m.}}$	W	ΔW
128	95	1.517	0.220
114	94	1.119	0.156
113	90	0.858	0.093
98	93	0.959	0.136
62	91	0.498	0.057
35	85	0.506	0.056

TABLE XVII. Angular correlation function W for different angles of the π^-. The corresponding π^+ momentum is $p_{\pi^+}^{\text{c.m.}} \in$ [89 MeV/c; 111 MeV/c], $\theta_{\pi^+}^{\text{c.m.}} = 73° \pm 10°$. The angles are given in degrees.

$\theta_{\pi^-}^{\text{c.m.}}$	$\phi_{\pi^-}^{\text{c.m.}}$	W	ΔW
115	176	2.982	0.184
116	168	2.835	0.167
116	152	2.502	0.163
117	128	2.033	0.105
117	111	1.687	0.089
115	92	0.908	0.073
115	72	0.575	0.091
115	62	0.427	0.096
116	49	0.391	0.065

TABLE XVIII. Angular correlation function W for different angles of the π^-. The corresponding π^+ momentum is $p_{\pi^+}^{\text{c.m.}} \in$ [89 MeV/c; 111 MeV/c], $\theta_{\pi^+}^{\text{c.m.}} = 73° \pm 10°$. The angles are given in degrees.

$\theta_{\pi^-}^{\text{c.m.}}$	$\phi_{\pi^-}^{\text{c.m.}}$	W	ΔW
91	174	3.012	0.168
92	160	2.756	0.130
96	125	2.177	0.197
97	109	1.510	0.149
99	93	0.883	0.119
93	58	0.394	0.060

TABLE XIX. Angular correlation function W for different angles of the π^-. The corresponding π^+ momentum is $p_{\pi^+}^{\mathrm{c.m.}} \in$ [89 MeV/c; 111 MeV/c], $\theta_{\pi^+}^{\mathrm{c.m.}} = 73° \pm 10°$. The angles are given in degrees.

$\theta_{\pi^-}^{\mathrm{c.m.}}$	$\phi_{\pi^-}^{\mathrm{c.m.}}$	W	ΔW
65	177	2.747	0.190
68	167	1.982	0.127
68	151	2.058	0.124
59	135	1.329	0.117
64	91	0.588	0.055
75	74	0.352	0.055
72	63	0.295	0.040
59	54	0.230	0.044
80	40	0.104	0.030

TABLE XX. Angular correlation function W for different angles of the π^-. The corresponding π^+ momentum is $p_{\pi^+}^{\mathrm{c.m.}} \in$ [89 MeV/c; 111 MeV/c], $\theta_{\pi^+}^{\mathrm{c.m.}} = 73° \pm 10°$. The angles are given in degrees.

$\theta_{\pi^-}^{\mathrm{c.m.}}$	$\phi_{\pi^-}^{\mathrm{c.m.}}$	W	ΔW
42	174	1.351	0.076
41	149	1.226	0.075
45	119	0.697	0.085
36	85	0.462	0.048
49	46	0.215	0.033
29	1	0.032	0.100

TABLE XXI. Angular correlation function W for different angles of the π^-. The corresponding π^+ momentum is $p_{\pi^+}^{\mathrm{c.m.}} \in$ [89 MeV/c; 111 MeV/c], $\theta_{\pi^+}^{\mathrm{c.m.}} = 73° \pm 10°$. The angles are given in degrees.

$\theta_{\pi^-}^{\mathrm{c.m.}}$	$\phi_{\pi^-}^{\mathrm{c.m.}}$	W	ΔW
157	174	1.821	0.171
141	175	2.677	0.178
123	176	2.985	0.280
108	176	2.980	0.243
91	174	3.012	0.168
67	174	2.579	0.152
46	177	1.723	0.132
28	176	0.904	0.095

TABLE XXII. Angular correlation function W for different angles of the π^-. The corresponding π^+ momentum is $p_{\pi^+}^{\mathrm{c.m.}} \in$ [89 MeV/c; 111 MeV/c], $\theta_{\pi^+}^{\mathrm{c.m.}} = 73° \pm 10°$. The angles are given in degrees.

$\theta_{\pi^-}^{\mathrm{c.m.}}$	$\phi_{\pi^-}^{\mathrm{c.m.}}$	W	ΔW
154	148	1.709	0.166
139	156	2.807	0.186
123	160	2.620	0.177
108	160	2.717	0.156
92	160	2.756	0.130
79	164	2.219	0.126
54	154	1.410	0.101
32	143	0.998	0.095

TABLE XXIII. Angular correlation function W for different angles of the π^-. The corresponding π^+ momentum is $p_{\pi^+}^{\mathrm{c.m.}} \in$ [89 MeV/c; 111 MeV/c], $\theta_{\pi^+}^{\mathrm{c.m.}} = 73° \pm 10°$. The angles are given in degrees.

$\theta_{\pi^-}^{\mathrm{c.m.}}$	$\phi_{\pi^-}^{\mathrm{c.m.}}$	W	ΔW
129	95	1.640	0.212
115	94	0.945	0.131
115	90	0.891	0.088
99	93	0.883	0.119
64	91	0.588	0.055
36	85	0.462	0.048

TABLE XXIV. Angular correlation function W for different angles of the π^-. The corresponding π^+ momentum is $p_{\pi^+}^{\mathrm{c.m.}} \in$ [102 MeV/c; 124 MeV/c], $\theta_{\pi^+}^{\mathrm{c.m.}} = 71° \pm 10°$. The angles are given in degrees.

$\theta_{\pi^-}^{\mathrm{c.m.}}$	$\phi_{\pi^-}^{\mathrm{c.m.}}$	W	ΔW
117	176	2.981	0.185
117	168	2.795	0.165
117	152	2.624	0.167
119	128	2.298	0.114
119	111	1.380	0.082
117	92	1.118	0.083
117	72	0.572	0.093
118	62	0.269	0.078
118	49	0.322	0.061

TABLE XXV. Angular correlation function W for different angles of the π^-. The corresponding π^+ momentum is $p_{\pi^+}^{\mathrm{c.m.}} \in$ [102 MeV/c; 124 MeV/c], $\theta_{\pi^+}^{\mathrm{c.m.}} = 71° \pm 10°$. The angles are given in degrees.

$\theta_{\pi^-}^{\mathrm{c.m.}}$	$\phi_{\pi^-}^{\mathrm{c.m.}}$	W	ΔW
93	174	2.872	0.163
94	160	3.205	0.141
98	125	2.340	0.203
99	109	1.495	0.149
102	93	1.150	0.136
96	58	0.430	0.062

TABLE XXVI. Angular correlation function W for different angles of the π^-. The corresponding π^+ momentum is $p_{\pi^+}^{\mathrm{c.m.}} \in$ [102 MeV/c; 124 MeV/c], $\theta_{\pi^+}^{\mathrm{c.m.}} = 71° \pm 10°$. The angles are given in degrees.

$\theta_{\pi^-}^{\mathrm{c.m.}}$	$\phi_{\pi^-}^{\mathrm{c.m.}}$	W	ΔW
66	177	2.515	0.180
69	167	2.263	0.134
69	151	1.955	0.120
60	135	1.477	0.122
65	91	0.558	0.053
77	74	0.497	0.064
75	63	0.366	0.044
61	54	0.317	0.050
83	40	0.126	0.033

TABLE XXVII. Angular correlation function W for different angles of the π^-. The corresponding π^+ momentum is $p_{\pi^+}^{\mathrm{c.m.}} \in$ [102 MeV/c; 124 MeV/c], $\theta_{\pi^+}^{\mathrm{c.m.}} = 71° \pm 10°$. The angles are given in degrees.

$\theta_{\pi^-}^{\mathrm{c.m.}}$	$\phi_{\pi^-}^{\mathrm{c.m.}}$	W	ΔW
43	174	1.154	0.069
42	149	1.225	0.073
46	119	0.813	0.089
37	85	0.406	0.043
51	46	0.179	0.029
30	1	0.030	0.100

TABLE XXVIII. Angular correlation function W for different angles of the π^-. The corresponding π^+ momentum is $p_{\pi^+}^{\mathrm{c.m.}} \in$ [102 MeV/c; 124 MeV/c], $\theta_{\pi^+}^{\mathrm{c.m.}} = 71° \pm 10°$. The angles are given in degrees.

$\theta_{\pi^-}^{\mathrm{c.m.}}$	$\phi_{\pi^-}^{\mathrm{c.m.}}$	W	ΔW
158	174	1.586	0.166
142	175	2.310	0.169
124	176	2.984	0.282
110	176	2.978	0.244
93	174	2.872	0.163
68	174	2.586	0.151
47	177	1.571	0.124
28	176	0.675	0.080

TABLE XXIX. Angular correlation function W for different angles of the π^-. The corresponding π^+ momentum is $p_{\pi^+}^{\mathrm{c.m.}} \in$ [102 MeV/c; 124 MeV/c], $\theta_{\pi^+}^{\mathrm{c.m.}} = 71° \pm 10°$. The angles are given in degrees.

$\theta_{\pi^-}^{\mathrm{c.m.}}$	$\phi_{\pi^-}^{\mathrm{c.m.}}$	W	ΔW
155	148	1.347	0.152
140	156	2.442	0.178
125	160	2.800	0.183
110	160	2.649	0.153
94	160	3.205	0.141
80	164	2.241	0.126
55	154	1.482	0.102
33	143	0.953	0.090

TABLE XXX. Angular correlation function W for different angles of the π^-. The corresponding π^+ momentum is $p_{\pi^+}^{\mathrm{c.m.}} \in$ [102 MeV/c; 124 MeV/c], $\theta_{\pi^+}^{\mathrm{c.m.}} = 71° \pm 10°$. The angles are given in degrees.

$\theta_{\pi^-}^{\mathrm{c.m.}}$	$\phi_{\pi^-}^{\mathrm{c.m.}}$	W	ΔW
131	95	1.492	0.207
117	94	1.213	0.152
117	90	1.074	0.098
102	93	1.150	0.136
65	91	0.558	0.053
37	85	0.406	0.043

TABLE XXXI. Angular correlation function W for different angles of the π^-. The corresponding π^+ momentum is $p_{\pi^+}^{\mathrm{c.m.}} \in$ [116 MeV/c; 138 MeV/c], $\theta_{\pi^+}^{\mathrm{c.m.}} = 69° \pm 10°$. The angles are given in degrees.

$\theta_{\pi^-}^{\mathrm{c.m.}}$	$\phi_{\pi^-}^{\mathrm{c.m.}}$	W	ΔW
119	176	3.011	0.190
119	168	2.918	0.175
120	152	2.493	0.168
122	128	2.178	0.114
122	111	1.372	0.085
120	92	1.026	0.083
121	72	0.416	0.085
121	62	0.316	0.091
122	49	0.335	0.069

TABLE XXXII. Angular correlation function W for different angles of the π^-. The corresponding π^+ momentum is $p_{\pi^+}^{\mathrm{c.m.}} \in$ [116 MeV/c; 138 MeV/c], $\theta_{\pi^+}^{\mathrm{c.m.}} = 69° \pm 10°$. The angles are given in degrees.

$\theta_{\pi^-}^{\mathrm{c.m.}}$	$\phi_{\pi^-}^{\mathrm{c.m.}}$	W	ΔW
95	174	3.092	0.171
96	160	2.955	0.136
101	125	2.107	0.196
102	109	1.409	0.149
105	93	0.728	0.109
101	58	0.442	0.065

TABLE XXXIII. Angular correlation function W for different angles of the π^-. The corresponding π^+ momentum is $p_{\pi^+}^{\mathrm{c.m.}} \in$ [116 MeV/c; 138 MeV/c], $\theta_{\pi^+}^{\mathrm{c.m.}} = 69° \pm 10°$. The angles are given in degrees.

$\theta_{\pi^-}^{\mathrm{c.m.}}$	$\phi_{\pi^-}^{\mathrm{c.m.}}$	W	ΔW
68	177	2.374	0.175
71	167	2.335	0.137
71	151	2.218	0.129
62	135	1.528	0.124
68	91	0.644	0.057
81	74	0.532	0.066
79	63	0.220	0.034
65	54	0.275	0.045
88	40	0.144	0.035

TABLE XXXIV. Angular correlation function W for different angles of the π^-. The corresponding π^+ momentum is $p_{\pi^+}^{\mathrm{c.m.}} \in$ [116 MeV/c; 138 MeV/c], $\theta_{\pi^+}^{\mathrm{c.m.}} = 69° \pm 10°$. The angles are given in degrees.

$\theta_{\pi^-}^{\mathrm{c.m.}}$	$\phi_{\pi^-}^{\mathrm{c.m.}}$	W	ΔW
45	174	1.194	0.070
43	149	1.188	0.072
48	119	0.814	0.088
39	85	0.476	0.046
54	46	0.192	0.029
32	1	0.027	0.100

TABLE XXXV. Angular correlation function W for different angles of the π^-. The corresponding π^+ momentum is $p_{\pi^+}^{\text{c.m.}} \in$ [116 MeV/c; 138 MeV/c], $\theta_{\pi^+}^{\text{c.m.}} = 69° \pm 10°$. The angles are given in degrees.

$\theta_{\pi^-}^{\text{c.m.}}$	$\phi_{\pi^-}^{\text{c.m.}}$	W	ΔW
161	178	1.717	0.300
144	175	1.915	0.166
126	176	2.636	0.270
112	176	3.299	0.265
95	174	3.092	0.171
70	174	2.351	0.144
49	177	1.417	0.118
29	176	0.867	0.090

TABLE XXXVI. Angular correlation function W for different angles of the π^-. The corresponding π^+ momentum is $p_{\pi^+}^{\text{c.m.}} \in$ [116 MeV/c; 138 MeV/c], $\theta_{\pi^+}^{\text{c.m.}} = 69° \pm 10°$. The angles are given in degrees.

$\theta_{\pi^-}^{\text{c.m.}}$	$\phi_{\pi^-}^{\text{c.m.}}$	W	ΔW
158	141	1.076	0.218
142	156	1.621	0.156
127	160	2.474	0.178
112	160	2.895	0.166
96	160	2.955	0.136
82	164	2.520	0.135
56	154	1.682	0.109
34	143	0.791	0.081

TABLE XXXVII. Angular correlation function W for different angles of the π^-. The corresponding π^+ momentum is $p_{\pi^+}^{\text{c.m.}} \in$ [116 MeV/c; 138 MeV/c], $\theta_{\pi^+}^{\text{c.m.}} = 69° \pm 10°$. The angles are given in degrees.

$\theta_{\pi^-}^{\text{c.m.}}$	$\phi_{\pi^-}^{\text{c.m.}}$	W	ΔW
134	95	0.767	0.158
121	94	1.005	0.145
120	90	1.036	0.102
105	93	0.728	0.109
68	91	0.644	0.057
39	85	0.476	0.046

TABLE XXXVIII. Angular correlation function W for different angles of the π^-. The corresponding π^+ momentum is $p_{\pi^+}^{\text{c.m.}} \in$ [129 MeV/c; 174 MeV/c], $\theta_{\pi^+}^{\text{c.m.}} = 67° \pm 10°$. The angles are given in degrees.

$\theta_{\pi^-}^{\text{c.m.}}$	$\phi_{\pi^-}^{\text{c.m.}}$	W	ΔW
124	176	2.696	0.198
124	168	2.941	0.203
124	153	2.256	0.184
126	128	2.048	0.132
126	111	1.294	0.105
124	92	0.920	0.105

TABLE XXXIX. Angular correlation function W for different angles of the π^-. The corresponding π^+ momentum is $p_{\pi^+}^{\text{c.m.}} \in$ [129 MeV/c; 174 MeV/c], $\theta_{\pi^+}^{\text{c.m.}} = 67° \pm 10°$. The angles are given in degrees.

$\theta_{\pi^-}^{\text{c.m.}}$	$\phi_{\pi^-}^{\text{c.m.}}$	W	ΔW
101	174	2.809	0.158
102	160	2.634	0.126
108	125	2.384	0.225
109	109	1.215	0.153
112	93	1.061	0.164
107	59	0.366	0.078

TABLE XL. Angular correlation function W for different angles of the π^-. The corresponding π^+ momentum is $p_{\pi^+}^{\text{c.m.}} \in$ [129 MeV/c; 174 MeV/c], $\theta_{\pi^+}^{\text{c.m.}} = 67° \pm 10°$. The angles are given in degrees.

$\theta_{\pi^-}^{\text{c.m.}}$	$\phi_{\pi^-}^{\text{c.m.}}$	W	ΔW
75	178	2.568	0.172
77	167	2.376	0.130
77	151	2.069	0.116
70	135	1.266	0.104
77	91	0.480	0.047
90	74	0.559	0.071
88	63	0.320	0.043
75	54	0.345	0.049
97	40	0.135	0.041

TABLE XLI. Angular correlation function W for different angles of the π^-. The corresponding π^+ momentum is $p_{\pi^+}^{\text{c.m.}} \in$ [129 MeV/c; 174 MeV/c], $\theta_{\pi^+}^{\text{c.m.}} = 67° \pm 10°$. The angles are given in degrees.

$\theta_{\pi^-}^{\text{c.m.}}$	$\phi_{\pi^-}^{\text{c.m.}}$	W	ΔW
50	175	1.202	0.063
50	149	1.127	0.062
56	119	0.722	0.074
48	85	0.402	0.036
65	46	0.184	0.026
54	1	0.015	0.100

TABLE XLII. Angular correlation function W for different angles of the π^-. The corresponding π^+ momentum is $p_{\pi^+}^{\text{c.m.}} \in$ [129 MeV/c; 174 MeV/c], $\theta_{\pi^+}^{\text{c.m.}} = 67° \pm 10°$. The angles are given in degrees.

$\theta_{\pi^-}^{\text{c.m.}}$	$\phi_{\pi^-}^{\text{c.m.}}$	W	ΔW
148	178	2.851	0.576
130	176	2.532	0.321
118	176	2.787	0.252
101	174	2.809	0.158
76	174	2.393	0.135
55	177	1.520	0.113
35	177	0.725	0.073

TABLE XLIII. Angular correlation function W for different angles of the π^-. The corresponding π^+ momentum is $p_{\pi^+}^{\text{c.m.}} \in$ [129 MeV/c; 174 MeV/c], $\theta_{\pi^+}^{\text{c.m.}} = 67° \pm 10°$. The angles are given in degrees.

$\theta_{\pi^-}^{\text{c.m.}}$	$\phi_{\pi^-}^{\text{c.m.}}$	W	ΔW
146	152	1.893	0.443
131	160	2.243	0.214
118	160	2.812	0.178
102	160	2.634	0.126
88	164	2.445	0.125
62	154	1.574	0.096
40	143	0.724	0.068

W function close together in the $(\theta_{\pi^-}, \phi_{\pi^-})$ plane, derived from a low number of events, were melted together for better statistics. This led to the total number of data points, listed in Tables III—XLIV. The W data are arranged in the tables in intervals of θ_{π^-} and ϕ_{π^-}, respectively. Therefore, the W function can be displayed versus the angle ϕ_{π^-} or θ_{π^-}. To demonstrate the variety of the data, Fig. 11 shows the selected Tables XXXI–XXXVII graphically.

2. The double differential cross section

Although the presented experiment was not designed for determining double differential cross sections, it delivered this observable for distinct combinations of momentum and angles. This provides the possibility to compare the data with other experiments [7, 10–12]. Because of the lack of triple differential cross section data or W-function data from other experiments, the comparison of double differential cross section results is an important check for the validity of the data.

The double differential cross section was extracted from the "free" event rate. This rate is well known, since the "free" events were taken during the complete experiment. This was possible because the restrictive first arm delivered an event rate which allowed one to take the free π^+ events simultaneously to the kinematically complete events.

The double differential cross section was obtained from the experimental values as demonstrated in Eq. (3.2). The c.m. values were derived from the laboratory values by well-known transformations.

TABLE XLIV. Angular correlation function W for different angles of the π^-. The corresponding π^+ momentum is $p_{\pi^+}^{\text{c.m.}} \in$ [129 MeV/c; 174 MeV/c], $\theta_{\pi^+}^{\text{c.m.}} = 67° \pm 10°$. The angles are given in degrees.

$\theta_{\pi^-}^{\text{c.m.}}$	$\phi_{\pi^-}^{\text{c.m.}}$	W	ΔW
136	96	1.529	0.468
125	94	0.903	0.209
123	90	0.925	0.122
112	93	1.061	0.164
77	91	0.480	0.047
48	85	0.402	0.036

Due to the large momentum acceptance of the used π^+ spectrometer, a reasonable momentum range of the π^+ was covered by one magnetic setting of the spectrometer magnet. The binning for the double differential cross section was set off-line to a reasonable value with respect to the number of taken events. The momentum intervals were chosen to be 10 MeV/c in the laboratory system. The most uncertain quantity in Eq. (3.2) is the acceptance of the spectrometer $\Delta\Omega_{\pi^+}$. The problem of the determination of the spectrometer efficiency was discussed in Sec. II C 3. For the calculation of the double differential cross section Monte Carlo data for the spectrometer acceptance were used. As discussed in Sec. II C 3 the agreement of these values with experimental checks is quite good for momenta above 110 MeV/c. For lower momenta the uncertainties of the experimental checks grow strongly with decreasing momentum.

The further experimental values needed in Eq. (3.2) could be derived more precisely: N_{tgt} was calculated by the density of hydrogen and the length of the target cell. The errors due to gaseous bubbles within the liquid hydrogen were estimated to be below 2%. This was done by a comparison of event rates at different cooling power for the target and measurements with polyethylene and graphite targets. The value is in good agreement with Ref. [24], where the same target system was used.

During the experiment, the technical parameters such as gas flow, high voltages, etc. were very carefully kept constant. Also, the on-line efficiencies of the MWPCs C_4, C_5, and C_6, defined by the percentage of particles having one hit in the chambers with respect to the total number of scintillator trigger events, were very thoroughly monitored. These rates were constant within 1% during the experiment. This is a strict indication that the real efficiencies for a single π^+ traversing the wire chambers remained constant. The chamber efficiency was evaluated carefully from runs at the beginning, the middle and the end of the experiment by preparing a sample of π^+ traversing the chambers. This off-line analysis used information from the stop-detector scintillators. Furthermore, the results were checked by tuning the beamline to low energy π^+ and testing each chamber separately with elastically scattered π^+ using a special, separate scintillator telescope.

Of course, several values representing the composition and intensity of the beam, such as production beam intensity, rates on the beam defining counters, and rates of the monitoring telescope were also supervised. The beam was reproducible in stability, position, and composition. The beam rate was 1–2 MHz (π^- at 400 MeV/c). Count rates were scaled in CAMAC scalers, which were read out and cleared from time to time by the on-line computer.

As described in Sec. II C 1, e^- and μ^- contamination of the beam were suppressed by hardware and software. The remaining fraction of μ^- was estimated to be 1%. Taking all systematic errors into account we conclude an overall normalization error of $\pm 14\%$ for the double differential cross section. This number results from the sum of the uncertainties mentioned above (10% for the acceptance, 2% for the target thickness, 1% for the chamber

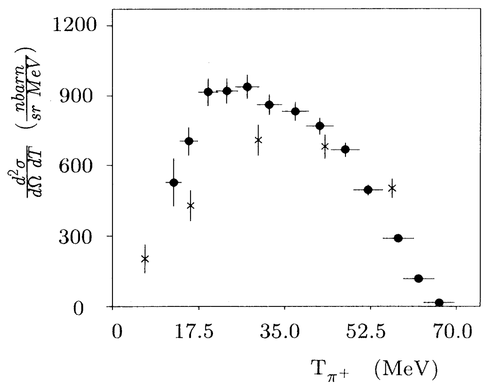

FIG. 12. Double differential cross section with statistical error as a function of the kinetic energy T of the π^+. The figure shows the comparison of this work (•) with Manley *et al.* (×) ([12]). The incoming energy of the π^- is 284 MeV (this work) and 280 MeV (Manley *et al.*). The polar angle region of the π^+ is $\cos\theta_{\pi^+} = 0.03$–$0.35$.

efficiencies, 1% for the beam normalization). Since the systematic errors may not cancel out by statistical fluctuation, the addition of all systematic errors seems to be justified. Because of the strongly dominating error in the acceptance we think that a sophisticated discussion of effects below 1% and their statistical independence is senseless. At very low energies a further systematic error due to the unknown behavior of the acceptance curve has to be added to the normalization errors: For data points with a π^+ kinetic energy below 45 MeV and below 32 MeV an additional systematic error of about 5% and 10%, respectively, may be assumed.

The data points are listed with the statistical errors in Table XLV. In addition, the behavior of the data versus the π^+ energy is shown in Fig. 12.

TABLE XLV. Double differential cross section $d^2\sigma/d\Omega_{\pi^+}dT_{\pi^+}$ versus the kinetic energy T_{π^+} of the π^+. The right side shows the statistical error $\Delta d^2\sigma/d\Omega_{\pi^+}dT_{\pi^+}$ and the width ΔT_{π^+} for the energy intervals. The systematic error for the double differential cross section is < 14% for all points. For data points with a π^+ kinetic energy below 45 MeV and below 32 MeV an additional systematic error of about 5% and 10% may be assumed, respectively.

T_{π^+} [MeV]	$d^2\sigma/d\Omega_{\pi^+}dT_{\pi^+}$ $[\frac{nb}{\mathrm{sr\ MeV}}]$	ΔT_{π^+} [MeV]	$\Delta d^2\sigma/d\Omega_{\pi^+}dT_{\pi^+}$ $[\frac{nb}{\mathrm{sr\ MeV}}]$
9.4	427	1.3	191
12.3	510	1.5	98
15.3	680	1.8	58
19.0	887	2.0	56
22.8	892	2.2	51
26.9	909	2.3	49
31.2	835	2.5	42
36.3	806	2.6	39
41.1	743	2.7	34
46.1	644	2.8	29
50.6	477	2.9	21
56.5	280	3.0	12
60.6	115	3.0	5
64.7	16	3.0	1

D. Checks of the experiment

As the presented experiment delivered only little redundant information to test the method of identification by means of kinematics, other consistency checks were performed:

Since a pure hydrogen target is the crucial point of the triggering of the experiment, an empty target run was performed. The rate of positive pions in the spectrometer nearly vanished and the reconstruction of the vertex point showed only the mylar walls of the target cell. No π^+ event was registered directly from inside the target cell, which proved the correctness of the track reconstruction and data evaluation algorithm. Unfortunately, the spacial resolution did not allow separating the limiting foils of the target cell completely. This caused a background of π^+ from the carbon within the Mylar foils via DCX and $(\pi, 2\pi)$ reactions. It turned out to be less than 1%. This value was determined by empty target measurements as well as by measurements with a graphite target. Moreover, this in any low background case was reduced dramatically by the requirement of a coincident charged particle in the π^- arm.

A subthreshold run with an incident beam energy of 2 MeV below threshold was performed with a full LH_2 target. It delivered a π^+-identification rate which was below 1%. This was comparable with the above-described empty target results. This π^+ source was mainly located at the carbon containing materials within the target (Mylar windows). Very few positive pions originated from the side parts of the cell. We suppose that this small fraction was caused by the widening and scattering of the π^- beam within the hydrogen. The beam slightly touched the Mylar foils of the target cell at the sides. Again, the coincidence of charged particles in the π^- arm strongly reduced this background.

This pionic background resulting from DCX reactions produced systematic errors in both the double differential cross section and the W function. Assuming a maximum error increase by nonisotropic momentum and angular distribution, a systematic error by non-$(\pi^- p \to \pi^+\pi^- n)$-reactions of less than 2% was estimated. This is negligible to the other errors.

The π^- arm was designed as a low cost large solid angle detector arrangement. Therefore, there was only one layer of scintillator and one low resolution wire chamber layer. The background free operation of the π^- arm in combination with the well-equipped spectrometer was thoroughly checked.

To check the level of spurious events in the π^+ arm, the rate of accidental events was measured by mismatching the timing (by integer multiple of the cyclotron pulse distance) of the two detector arms. It was less than 1%.

In order to trace the π^- tracks, a second wire chamber was mounted in front of a panel. The low background

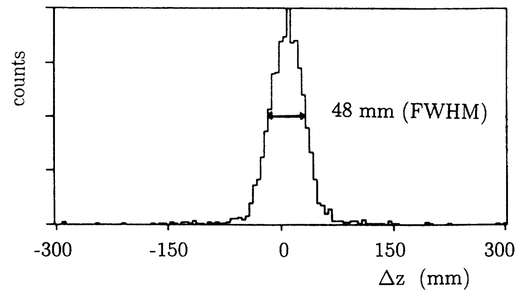

FIG. 13. This figure shows the mismatch distribution ($z_{\pi^+} - z_{\pi^-}$) of the vertex points seen by the π^+ and the π^- arm. The resolution of 48 mm is caused by the rough spatial resolution of the second arm chamber setup.

from spurious particles and accidental events is demonstated in Fig. 13. It shows the difference of the z coordinate of vertex points separately determined from the π^+ and π^- arm. In both cases, the vertex was defined by the intersection of the track with the z axis [(z,y) plane]. The distribution is dominated by the resolution of the wire chambers in the π^- arm, and a detailed analysis is consistent with the wire spacing and geometric arrangement of the chambers. Especially, the resolution of the two MWPCs with 1 cm wire gap was sufficient to locate the vertex point roughly in the target cell. The few points which seem to come from outside the target may be explained by misleading muon-tracks from decayed pions. A cut in Fig. 13 delivered an upper limit of 1.2% spurious particles.

To check the application of the $(\pi,2\pi)$ kinematics to the "complete" events the kinematical results for the velocity of the second charged particle was compared with the measured time of flight. The distribution of the time deviation (measured by time of flight minus kinematics calculations) was nearly Gaussian shaped, was centered at 0, and had a width of 1.2 ns (FWHM). This width is broader than the 850 ps detector resolution, which can be explained by the uncertainties in track length, multiple scattering, and pion decay.

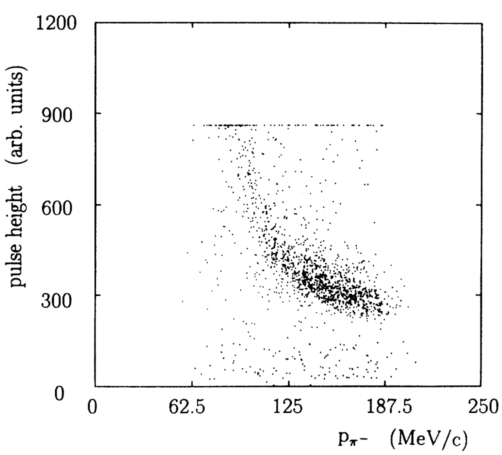

FIG. 14. Correlation between π^- momentum calculated by $(\pi,2\pi)$ kinematics and the pulse height of the scintillator. The distribution of the point density is according to a normal behavior of charged particles traversing a thin scintillator. In addition, there is a diffuse background caused by π^--annihilation reactions.

Furthermore, as demonstrated in Fig. 14, the pulse height distribution in the second arm scintillator plates was compared to the momentum delivered from kinematics for each event. Apparently, no events were detected with a momentum below 50 MeV/c. This is due to the stopping power of the target. This indicates the validity of the application of the $(\pi,2\pi)$ kinematics to the events. The "banana" shown in Fig. 14 is specific to the energy loss of the π^- within 2 cm plastic scintillator. The diffuse distribution of events around the "banana" is normal for the pulse heights of low energy negative pions. This is due to the neutral reactions and pion absorption channels of the pions within the scintillators. The shape of the distribution was checked with experiments performed at a very low energy π^- beam [25].

E. Comparison with other experiments

This is the first measurement of triple differential cross sections for $\pi^-p \to \pi^+\pi^-n$ in the resonance region. Therefore, no direct comparison of this observable to other experiments is possible. However, more inclusive information on $\pi^-p \to \pi^+\pi^-n$ were published and may in principle be extracted from the database of this experiment by integration. Since these data do not cover the complete phase space, an integration to comparable published data succeeds only for very specific kinematical conditions.

An example is the double differential cross section $\frac{d^2\sigma}{d\Omega_{\pi^+}dT_{\pi^+}}$ as a function of the kinetic energy T_{π^+} of the outgoing π^+. Figure 12 shows the data of this experiment together with results of Ref. [12]. It should be mentioned that the data of the two measurements were not taken exactly under the same conditions: the incident pion kinetic energy for our data is 284 MeV, whereas the data of Manley *et al.* were derived at 280 MeV at slightly different angles. Taking a scaling factor of about 10% for the different beam energies into account, the difference in the amplitude of both measurements is quite small. The difference in shape becomes less severe, when the different laboratory angles of both data sets are considered. With respect to the usual uncertainties of such spectrometer experiments at low pion energies the data of both experiments fit together quite well.

As a consequence, the integral of the measured curves is also identical within a 10% scaling error. This indicates that the data of this experiment agree with the total cross section data of Ref. [12].

F. Discussion of the results

The W function is not affected by eventually remaining scaling errors due to spectrometer acceptance, target thickness, etc. (see Sec. III) like in the double differential cross section. The independence of our main observable, the W function, on acceptance errors in the π^+ arm invites the W function to be used as a powerful tool for the study of the reaction dynamics.

As a first step to get information on the dynamics of the reaction, the data at the total c.m. energy of 1301 MeV for the W function were compared to the well-known kinematical phase space. The θ_{π^-} dependence (for $\phi_{\pi^-} = 175°$) and the ϕ_{π^-} dependence (for $\theta_{\pi^-} = 115°$) of the W-function data and the related phase space distribution are demonstrated in Fig. 15. The polar angle of the π^+ in the c.m. frame is fixed to $\theta_{\pi^+} = 78°$ (by the laboratory angle spectrometer position). The azimuthal angle ϕ_{π^+} is defined to be zero in our coordinate system. For this comparison, the momentum of the π^+ was chosen to be $p_{\pi^+} = 112$ MeV/c, as it turned out, so that the dependence of W on p_{π^+} is rather smooth (see Tables III–XLIV). One of the most striking features of this comparison is the strong deviation from phase space and the characteristic structure of the data. Evidently, the production process is strongly influenced by the underlying dynamics.

To get some more insight into this reaction dynamics, a closer look at some of the theoretical attempts is taken. A first attempt are the well-known graphs for s- and p-wave πN scattering, supplemented by one additional πNN vertex. These "classical" diagrams only involve a linear πN coupling, where the so-called p-wave term (referring to [16, 17]), including two baryonic intermediate states, dominates. Calculations of the expected behavior of the presented W-function data—especially the θ and ϕ dependence—were published by Jäkel *et al.* [17, 26]. The comparison of our data with this calculation, considering only the "classical" terms, shows a characteristic deviation of the structure (Fig. 16) in the θ_{π^-} as well as in the ϕ_{π^-} dependence.

However, it is well known that nonlinear diagrams also are important for the dynamics of pion production reactions. Therefore, these nonlinear terms, namely the pole and the contact term (referring to [16, 17]), are included in refined models for describing $(\pi, 2\pi)$ reactions [4, 16, 17, 27, 28]. Considering only these nonlinear terms, which should be dominated by the pole term, the calculations of the W function [17] also do not agree with the experimental data (Fig. 16). Thus, neither the nonlinear diagrams nor the linear diagrams alone can explain the dynamics of the reaction $\pi^- p \rightarrow \pi^+\pi^- n$, at least in this energy range close to the $\pi\pi$ threshold. Consequently, the linear and nonlinear diagrams enter into the theoretical models ([16, 17]).

The main result demonstrated in Fig. 16 is the good

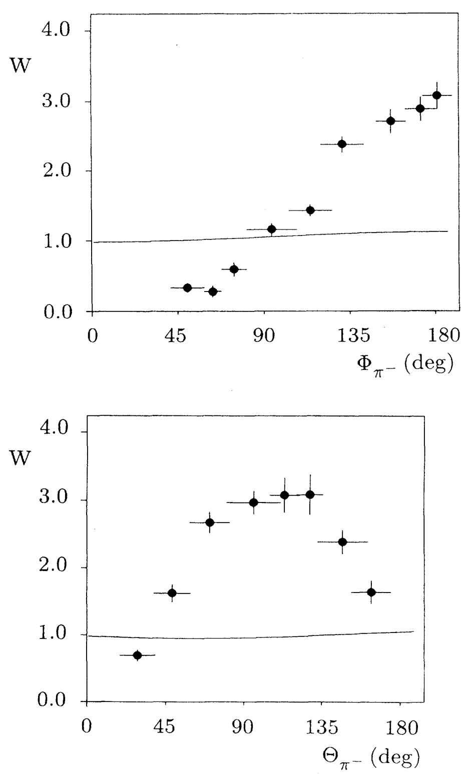

FIG. 15. Angular correlation function W as a function of the π^- azimuthal angle ($\theta_{\pi^-} = 115°$) and polar angle ($\phi_{\pi^-} = 175°$). The solid line indicates the phase space distribution. The kinematical variables have been fixed to $p_{\pi^+} = 112$ MeV/c, $\theta_{\pi^+} = 78°$, and $T_{\rm in}^{\rm lab} = 284$ MeV.

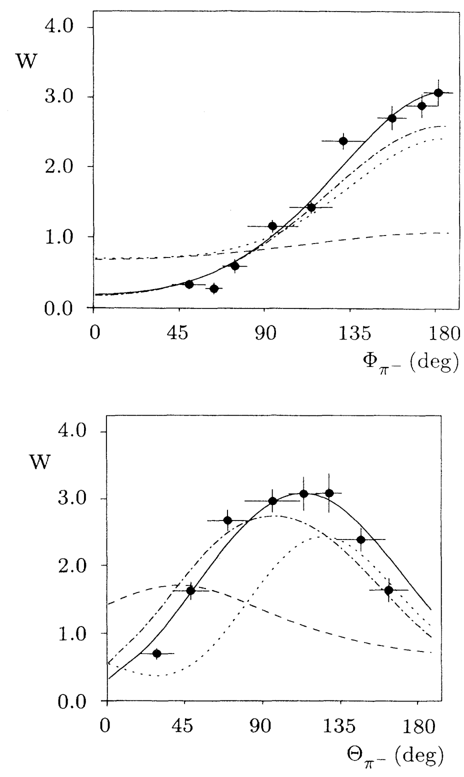

FIG. 16. Angular correlation function W as a function of the π^- azimuthal angle ($\theta_{\pi^-} = 115°$) and polar angle ($\phi_{\pi^-} = 175°$). The full solid line shows the result of the nonstatic calculations including linear and nonlinear terms. It was calculated by Jäkel *et al.* [26]. The dash-dotted line indicates the interference of all terms in the static limit. The dotted line includes only the resonance term and the dashed line only the pole term. The kinematical variables were fixed to $p_{\pi^+} = 112$ MeV/c, $\theta_{\pi^+} = 78,°$ and $T_{\rm in}^{\rm lab} = 284$ MeV.

agreement of our W-function data with the calculations of Ref. [17], based on the interference of the linear (s and p wave) and the nonlinear (pole and contact) terms. Thus, the dynamics of this pion production reaction is evidently dominated by the interference of linear and nonlinear contributions. It should be stressed that these calculations were realized before the data were known.

Although the calculations in Ref. [17] describe the data qualitatively, the experiment shows an even more pronounced structure. However, the above-mentioned calculations have been worked out in the static limit; i.e., the recoil of the baryon has been neglected. In a refined model [26] the calculations were performed in a nonstatic approach. These calculations are compared to experiment in Fig. 16, where the agreement of data and model is excellent. Therefore, it must be concluded that even in the energy region near the $\pi\pi$ threshold, relativistic effects are important for a good description of the dynamics. In addition, corrections from initial and final state interactions are small according to this model.

Recent experiments like Saxon *et al.* [9] and the OMICRON Collaboration [14] conclude from their data the existence of a $J^{PC} = 0^{++}$ isoscalar $\pi\pi$ resonance in the near threshold energy region that would dominate the dynamics of the pion production process in this isospin channel. This statement is based on invariant mass spectra extracted from the experimental data, a quantity which is less exclusive than the W function. This quantity has also been calculated by Jäkel *et al.* [29], where linear and nonlinear diagrams as well as relativistic corrections were considered. Figure 17 shows the good agreement of the model with our invariant mass spectrum, which matches qualitatively with other experiments. In addition, this structure also shows up in an independent calculation of Oset and Vicente-Vacas, who also combined linear and nonlinear terms in their model (see Fig. 15 of Ref. [16]).

Thus, the main result is that the peaklike behavior at the upper $\pi\pi N$ phase space limit results from the interference of linear and nonlinear diagrams. This causes the pronunciation of back-to-back pion events and, consequently, the formation of dominantly large invariant masses. As a consequence, the data do not support a $\pi\pi$ resonance with a width in the order of the considered invariant mass region. This finding is in line with the fact that the position and the width of the resonancelike peak in the invariant mass spectra change with the incoming energy, as can be seen in Refs. [9] and [14].

Summarizing, we conclude that the dynamics of the reaction $\pi^- p \rightarrow \pi^+\pi^- n$ is well described within the framework of models based on Weinberg's Lagrangian, as in Refs. [17, 16, 26]; that there are clear indications that relativistic corrections near threshold are not negligible; that a description of the data is possible without the need for initial and final state interactions induced by σ and ρ propagation; and that the invariant mass distribution does not support a new isoscalar $\pi\pi$ resonance.

Since in this paper all data and calculations were worked out at a total c.m. energy $E_{\mathrm{c.m.}} = 1301$ MeV, no firm conclusions on the energy dependence of the dynamics of this reaction can be made at the moment. However, to fix the energy dependence of W function, data at the two energies $E_{\mathrm{c.m.}} = 1284$ MeV and $E_{\mathrm{c.m.}} = 1334$ MeV for the reaction $\pi^- p \rightarrow \pi^+\pi^- n$ have been taken. The results will be reported explicitly in a forthcoming publication.

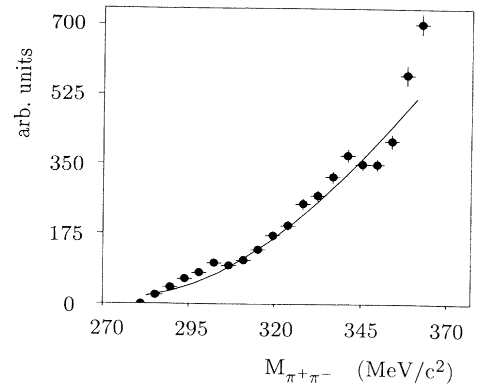

FIG. 17. Distribution of the measured $\pi^+\pi^-$ invariant mass spectrum divided by the accepted phase space. The bars demonstrate the statistical error. The full line shows the result of the nonstatic calculations of Jäkel *et al.* [26].

ACKNOWLEDGMENTS

The authors would like to acknowledge the help of W. Kluge, H. Matthäy, D. Renker, T. Raab, and all the people at the Paul Scherrer Institute for their interest and support for this experiment. Special thanks are also due to M. Dillig for his continuous cooperation and interest in this experiment.

[1] A. Chodos and C.B. Thorn, Phys. Rev. D **12**, 2733 (1975); T. Inoue and T. Maskawa, Prog. Theor. Phys. **54**, 1833 (1975); G.E. Brown and M. Rho, Phys. Lett. **82B**, 177 (1979); G.E. Brown, M. Rho, and V. Vento, *ibid.* **84B**, 383 (1979); C.G. Callan, R.F. Dashen, and D.H. Gross, Phys. Rev. D **19**, 1826 (1979); I. Hultage, F. Myhrer, and Z. Xu, Nucl. Phys. **A364**, 322 (1981); A.W. Thomas, Adv. Nucl. Phys. **13**, 1 (1983); J. Phys. G **7** L283 (1981); S. Theberge, Phys. Rev. D **22**, 2811 (1980); **23**, 2106 (1981).

[2] *Current Algebra*, edited by S. Adler and R. Dashen (Benjamin, New York, 1968); S. Weinberg, Phys. Rev. Lett. **17**, 616 (1966); L. Turner, Nucl. Phys. **B11**, 355 (1969).

[3] J. Gasser and H. Leutwyler, Phys. Rep. **87** C, 77 (1982); Phys. Lett. **125B**, 321 (1983); **125B**, 325 (1983); Ann. Phys. **158**, 142 (1984).

[4] S. Weinberg, Phys. Rev. Lett. **18**, 168 (1967); Phys. Rev. **166**, 1568 (1968); Phys. Rev. Lett. **17**, 616 (1966).

[5] Yu.A. Batusov, S.A. Bunyatov, V.M. Sidorov, and V.A. Yarba, Zh. Eksp. Teor. Fiz. **43**, 2015 (1962) [Sov. Phys.

JETP **16**, 1422 (1963)]; Yad. Fiz. **1**, 687 (1965) [Sov. J. Nucl. Phys. **1**, 492 (1965)]; *ibid.* **5**, 1060 (1967) [Sov. J. Nucl. Phys. **5**, 757 (1967)].

[6] M. Blau and M. Caulton, Phys. Rev. **96**, 150 (1954); J. Crussard *et al.*, *ibid.* **94**, 736 (1954); W.D. Walker, J. Crussard, Phys. Rev. **98**, 1416 (1955).

[7] W.A. Perkins III, J.C. Caris, R.W. Kenney, and V. Perez-Mendez, Phys. Rev. **118**, 1364 (1960).

[8] J. Kirz, J. Schwartz, and D. Tripp, Phys. Rev. **130**, 2481 (1963).

[9] D.H. Saxon and J.H. Mulvey, Phys. Rev. D **2**, 1790 (1970); J.A. Jones, W.W.M. Allison, and D.H. Saxon, Nucl. Phys. **B83**, 93 (1974).

[10] B.C. Barish, R.J. Kurz, P.G. McManigal, V. Perez-Mendez, and J. Solomon, Phys. Rev. Lett. **6**, 297 (1961); B.C. Barish, R.J. Kurz, P.G. McManigal, V. Perez-Mendez, and J. Solomon, Phys. Rev. **135**, 416 (1964).

[11] C.W. Bjork, S.E. Jones, T.R. King, D.M. Manley, A.T. Oyer, G.A. Rebka, Jr., J.B. Walter, R. Carawon, P.A.M. Gram, F.T. Shively, C.A. Bordner, and E.L. Loman, Phys. Rev. Lett. **44**, 62 (1980).

[12] D.M. Manley, Phys. Rev. D **30**, 536 (1984); **30**, 904 (1984); Los Alamos Report LA-9101-T, 1981 (unpublished).

[13] A. Aaron *et al.*, Phys. Rev. Lett. **44**, 66 (1980); V.G. Zinov and S.M. Korenchenko, Zh. Eksp. Teor. Fiz. **34**, 301 (1958) [Sov. Phys. JETP **34**, 210 (1958)].

[14] OMICRON Collaboration, Phys. Lett. B **216**, 244 (1989); Phys. Lett. B **225**, 198 (1989); Z. Phys. C **48**, 201 (1990); **51**, 377 (1991); Reports CERN-EP/89-104 (1989), CERN-EP/88-116 (1988), and CERN-EP/88-140 (1988).

[15] H.-W. Ortner, R. Baran, U. Bohnert, M. Dillig, G. Herrmann, A. Hofmann, P. Helbig, O. Jäkel, W. Kluge, H. Krüger, D. Malz, H. Matthäy, R. Müller, W. Menzel, L. Schweinzer, and S. Wirth, Phys. Rev. Lett. **64**, 2759 (1990).

[16] E. Oset and M.J. Vincente-Vacas, Nucl. Phys. **A446**, 584 (1985).

[17] O. Jäkel, H.W. Ortner, M. Dillig, and C.A.Z. Vasconcellos, Nucl. Phys. **A511**, 733 (1990).

[18] *SIN-Users Handbook* (Schweizer Institut für Nuklearforschung, Villigen, 1981).

[19] H.W. Ortner, D. Malz, and R. Müller, J. Vac. Sci. Technol. **A8**(4), 3370 (1990).

[20] V.L. Highland, Nucl. Instrum. Methods. **129**, 497 (1975); **161**, 171 (1979).

[21] W.T. Scott, Rev. Mod. Phys. **35**, 231 (1963); J.W. Motz, H. Olson, and H.W. Koch, *ibid.* **36**, 881 (1964).

[22] J.T. Brack *et al.*, Phys. Rev. C **34**, 1771 (1986), and references therein.

[23] J. Julien, M. Bolove, X. Charlot, J. Girard, G.S. Pappalardo, J. Poiton, and L. Roussel, Trans. Nucl. Sci. Vol. **NS-31**, No. 1, 129 (1984).

[24] R.F. Jenefsky *et al.*, Nucl. Phys. **A290**, 407 (1977); M.T. Tran *et al.*, *ibid.* **A324**, 301 (1979).

[25] T. Johannson, private communication.

[26] O. Jäkel, M. Dillig, and C.A.Z. Vasconcellos, Nucl. Phys. **A541**, 675 (1992).

[27] M.G. Olsson and L. Turner, Phys. Rev. Lett. **20**, 1127 (1968); Phys. Rev. **181**, 2141 (1969); Phys. Rev. D **6**, 3522 (1972); L. Turner; Nucl. Phys. **B11**, 355 (1969); J. Schwinger, Phys. Lett. **24B**, 473 (1967).

[28] R.A. Arndt, J.B. Cammarate, Y.N. Goradia, R.H. Hackman, and V.L. Teplitz, Phys. Rev. D **20**, 651 (1979); R.S. Bhalerao and L.C. Liu, **30**, 224 (1984).

[29] O. Jäkel and M. Dillig (unpublished).

[30] M. Gell-Mann and M. Levy, Nuovo Cim. **16**, 705 (1960).